

MAX-PLANCK-INSTITUT FÜR PLASMAPHYSIK
GARCHING BEI MÜNCHEN

SECOND HARMONIC ION CYCLOTRON RESONANCE
HEATING IN ASDEX: RESULTS OF RAY TRACING
CALCULATIONS

K. Steinmetz, M. Brambilla

IPP 4/219

July 1984

*Die nachstehende Arbeit wurde im Rahmen des Vertrages zwischen dem
Max-Planck-Institut für Plasmaphysik und der Europäischen Atomgemeinschaft über die
Zusammenarbeit auf dem Gebiete der Plasmaphysik durchgeführt.*

IPP 4/219

K. Steinmetz
M. Brambilla

Second Harmonic Ion Cyclotron
Resonance Heating in ASDEX:
Results of Ray Tracing
Calculations

July 1984

Abstract

First ray tracing computations based on typical ASDEX hydrogen plasma parameters are presented. It is shown that the heating efficiency is already appreciable for ohmically heated discharges, where, depending on density, 10 to 25% single transit absorption has been calculated. The efficiency strongly increases with electron density and plasma temperature reaching more than 40% single transit absorption at $T_{i0} = 3$ keV, $T_{e0} = 1.5$ keV, $n_{e0} = 5 \times 10^{13} \text{ cm}^{-3}$. Well defined power deposition profiles with peak power densities of a few W/cm^3 per MW and of small halfwidth are found to be rather insensitive to typically observed variations of plasma density and temperature profiles. In the temperature range explored so far most wave power is transferred to the plasma ions.

1. INTRODUCTION

Recent experimental investigations at PLT, JFT-2/M and TFR /1-4/ have demonstrated the high heating potential of ICRF experiments performed either in two-ion schemes (mode conversion and minority regime) or at the second harmonic frequency of the majority ion species. Particularly second harmonic heating now looks very appealing since

- i) higher frequencies generally afford the possibility of applying wave guides or cavity antennae as launchers, and
- ii) experiments indicate that the wave power absorption is already appreciable under ohmic discharge conditions. In addition, present-day tokamak experiments do not possess sufficient radiation shielding and so working at high bulk plasma temperatures (multi-keV range) with hydrogen majority heating is safer and convenient.

Various ICRF experiments are now being conducted and increasing efforts are devoted to the preparation of high-power ICRF heating projects (ASDEX, ASDEX-UPGRADE, DIII-2, JET, JT-60, PLT, TEXTOR, TORE SUPRA etc.). ICRH in ASDEX is scheduled for operation in fall 1984. A total rf power of up to 3 MW within the frequency range 30 to 115 MHz will be available for pulse lengths of up to 10 sec /5, 6/. This wide range of frequencies allows us to work at two-ion heating schemes as well as at the second harmonic frequency of hydrogen which is supposed to have first priority in the experimental program of ASDEX.

The principles of ICRF heating and the heating mechanisms itself have been extensively analyzed /7-15/. Among various approaches ray tracing of ion

cyclotron waves has been shown to be a valuable tool in describing ICRF heating in medium and large tokamaks /16-20/, though - of course - not all observations of rf heating experiments can be explained in detail by it. However, if the inherent limitations of ray tracing are kept in mind, this approach - particularly when coupled to a transport code - allows a more profound understanding of ICRF heating in tokamak devices.

2. MODEL

The RAYIC code /21/ models coupling, propagation and absorption of e.m. waves in large axisymmetric plasmas in the ion cyclotron frequency domain. It combines a careful application of the Eikonal approximation (ray tracing and power transport) with a 3-D semianalytic solution of the Maxwell equations near the antenna and around singular layers (ion cyclotron and two-ion hybrid resonances). The code can thus be used to obtain detailed information both on the propagation of the waves and on the power deposition profiles, under a large range of conditions.

The core of the code is a ray tracing subroutine which follows the propagation of the fast (compressional) Alfvén wave in an arbitrarily axisymmetric configuration /16/. The plasma dispersion relation is written in the warm plasma approximation, the electron inertia being neglected.

The initial conditions for the ray and power transport equations are provided by a 3-D plane layered model of the antenna, described in /16/. The output of the antenna subroutine consists of the spectral distribution

of the radiated power among partial waves with different toroidal wave number n_ϕ , and, for each n_ϕ , the distribution of the power flux across a wave front in the poloidal direction. The power transport equation takes into account cyclotron damping at the fundamental and at the second harmonic resonances, and electron Landau and transit time damping. A detailed description of the treatment of the power absorption equation within singular layers is given in /16, 17/.

The limitations of the model are well known /16, 17/:

- a) Ray tracing generally cannot include diffraction effects and consequently cannot account for energy transferred to surface waves.
- b) The plasma must be large and dense enough to accommodate at least a few wavelengths in radial direction:

$$k_\perp \cdot a \gg 1$$

where a is the plasma minor radius. In the case of ASDEX this requirement is reasonably well fulfilled, i.e. $k_\perp \cdot a \approx 20$ within the region where ray tracing is applied.

- c) In addition, the power balance is only reliable if absorption is sufficiently strong, since selective eigenmode excitation cannot be taken into account.

Thus, while ray tracing in its present form cannot provide a complete description of ICRH, it is still a useful tool for describing the main

features of ICRH in present day tokamaks /22/. The main purpose of ray tracing computations - in our opinion - is not only the calculation of the absolute power absorption but also, and this may be even more important, to reach a more profound physical understanding of ICRH in toroidal plasmas, and to evaluate the inherent scaling of the various processes involved. It is obvious that the limitations of the ray tracing approach have always to be kept in mind when the results are being interpreted.

Before the results of the calculations are presented the dispersion relation should be considered. Figure 1 gives the radial dependence of the square of the perpendicular index n_{\perp} which is computed by the full hot plasma dispersion relation /23/ for $n_{\parallel} = 3$. The frequency of $f = 70$ MHz and the central toroidal magnetic field $B_T = 2.2$ T correspond to $\omega = 2\Omega_{CH}$ on axis in a pure hydrogen plasma, while the plasma parameters (central values and profiles) are typical of ohmic ASDEX discharges. A more detailed view on the variation of n_{\perp} around the resonance layer is given in Fig. 2. Though the resonance frequency of the second harmonic for hydrogen is located exactly on axis, the maximum of the absorption is slightly shifted out of axis towards the inside of the plasma.

3. DATA AND PARAMETERS

The computations are based on the following ASDEX and ICRF system parameters (Tables 1 and 2):

Minor radius $a = 40$ cm, major radius $R = 165$ cm, toroidal magnetic field $B_T = 2.3$ T, plasma current 250 to 450 kA. The density and temperature profiles were taken from experimental data. The frequency was $f = 70$ MHz, which places the $\omega = 2\Omega_{CH}$ layer of a hydrogen plasma just in the centre of the device. At this frequency, the average wavelength of the fast wave in the plasma is $\lambda \approx 10$ cm at $n_e = 5 \times 10^{13}$ cm $^{-3}$; the Eikonal approximation can thus be applied, albeit not by a large margin. We followed the waves for only one transit through the plasma, since standing wave effects cannot be taken into account by the model.

A power $P_{rf} = 1$ MW is assumed to be launched by a number of $\lambda/2$ -double antennae located on the low magnetic field side of the torus. They are described in detail in Ref. /24/. Figure 3 shows the geometry of one antenna in the poloidal plane. The width of one element in the toroidal direction, 18 cm, is such that a broad spectrum of partial waves with toroidal wave number n_ϕ up to about 40 is excited; the power spectrum is shown in Fig. 4. Only even modes $n_\phi = 0, 2, 4, 6 \dots 40$ were evaluated, corresponding to two toroidally opposite antennae such as will be used in the experiment. Figure 3 also shows one example of the propagation (rays and wave fronts) of the toroidal mode $n_\phi = 4$. The length of the arrows on the first wave front is proportional to the power flux through the corresponding poloidal section of the wave front.

4. RESULTS

4.1 ICRH with ohmic target plasma

Under ohmic discharge conditions ($n_{e0} = 5 \times 10^{13} \text{ cm}^{-3}$, $T_{e0} = 700 \text{ eV}$, $T_{i0} = 500 \text{ eV}$) about 14% of the launched power is absorbed in a single transit (Fig. 5, dashed line). Of this about three quarters (110 kW) goes to the ions through IC damping, and about one quarter (32 kW) to the electrons through electron Landau damping of the Bernstein wave excited by linear conversion just beyond the $\omega = 2\Omega_{CH}$ layer. Figure 6 shows that mode conversion is only effective for modes up to $n_\phi = 4$. Though relative modest, this value of the total single transit absorption is already sufficient to exclude high quality cavity mode excitation, which is important with respect to the validity of the antenna model and the power balance.

As expected, the absorption efficiency shows a marked dependence on the density and temperature (Fig. 5, 8), being in first approximation proportional to B , i.e. to the product nT . However, it can be shown that higher densities and particularly higher temperatures favour mode conversion of partial waves with low to moderate n_ϕ into ion Bernstein waves/25/; this in turn slightly increases the proportion of electron heating at the expense of ion heating. For effective mode conversion the evanescence layer has to be clearly separated from the IC-resonance layer. Since Doppler broadening is proportional to $n_{||} T^{1/2}$ /26/, while the width of the evanescence layer is proportional to $n_e T$, mode conversion is effective if $\text{const} \cdot n_{||} T^{1/2} < \text{const} \cdot n_e T$, where $n_{||} \approx \frac{c}{\omega} (n_\phi / R + B_p k_x / B_T)$.

This means that, n_ϕ must be sufficiently small, though the maximum permissible n_ϕ -value grows as the temperature.

This behaviour is in fact found in the numerical results shown in Figs. 5 and 7 where the density dependence of the heating efficiency at constant temperature is plotted. A more detailed analysis of the mode behaviour is displayed in Fig. 7, where the increase of the power deposited into the electrons in the density range $n_{e0} = 4$ to $5 \times 10^{13} \text{ cm}^{-3}$ corresponds to the transition of the $n_\phi = 4$ mode from the IC damping regime to the mode conversion regime, thereby reducing the absorption by the ions and, in turn, increasing the absorption by electron Landau damping. At higher densities, around $n_{e0} = 6$ to $7 \times 10^{13} \text{ cm}^{-3}$, the same effect occurs but then for the partial wave $n_\phi = 6$.

4.2 ICRH with preheated target plasma

The dependence of the heating efficiency on the ion temperature is presented in Fig. 8. At medium central density, $n_{e0} = 5 \times 10^{13} \text{ cm}^{-3}$, preheated plasmas absorb the radio frequency power fairly well. At $T_{i0} = 3 \text{ keV}$, $T_{e0} = 1.5 \text{ keV}$ corresponding to, for example, neutral beam preheated discharge conditions, up to 43% of the coupled power can be absorbed in a single transit. Of this, about one fifth (100 kW) is transferred to the electrons, and the rest (340 kW) to the ions. In this temperature range, direct electron transit time damping of the fast wave is still quite small, so that the fraction of power taken by the electrons is rather insensitive to the electron temperature and depends mainly (at constant density) on the ion temperature. This is also demonstrated in Fig. 8 where the calculations

with fixed (low) electron temperature show only slight differences to the results with varying T_{e0} .

A more detailed analysis of the temperature dependence of different modes is given in Fig. 9. Thus, between $T_{i0} = 1.5$ keV and 2.0 keV the partial wave $n_\phi = 8$ changes to the mode conversion regime, again increasing P_e and decreasing the slope of $P_{H+}(T_{i0})$ (Fig. 9) in a stepwise manner. At higher temperatures, however, the optical thickness of the evanescence layer associated with wave transformation is already larger than the optimum, so that P_e almost saturates. The next mode, $n_\phi = 10$, remains in the IC damping dominated regime up to $T_{i0} \approx 2.4$ keV. Absorption of higher n_ϕ -modes ($n_\phi \geq 12$) is still roughly proportional to T_i up to the highest temperature explored, $T_{i0} = 3$ keV. The wiggle of $P_{H+}(T_{i0})$ at the transitions is probably a numerical effect related to the difficulties encountered by the code in properly recognizing the various regimes, when used near the limits of applicability of the Eikonal approximation.

A summary of the behaviour of different n_ϕ -modes is displayed in Fig. 10. As already mentioned, at low temperatures (ohmically heated plasma) electron absorption is significant up to $n_\phi = 4$, while at higher temperatures corresponding to beam heated discharges it extends up to $n_\phi = 10$. The increase in IC absorption efficiency of high n_ϕ -modes with temperature is also evident from this figure.

For effective IC damping the Doppler broadening of the IC resonance layer has to be large enough to overlap with the evanescence layer, i.e.

$$\text{const} \cdot n_{\parallel} T^{1/2} > \text{const} \cdot n_e T.$$

So, for higher values of n_ϕ ($n_{||}$) the IC absorption will increase. Since mode conversion is most efficient at low to moderate n_ϕ the net effect is a strong IC damping at n_ϕ -values above the limit for mode conversion, particularly at higher temperatures. The modest absorption of high- n_ϕ modes ($n_\phi > 14$) by the electrons at $T_{i0} = 3$ keV, $T_{e0} = 1.5$ keV is due to the incipient transit time damping, not localized near the resonance layer.

4.3 Power deposition profiles

One of the main goals of ray tracing is to compute the power deposition profiles. However, the strong focussing seen in Fig. 3 makes the evaluation of power deposition profiles somewhat questionable. In the code, the problem has been dealt with by broadening the illuminated region over one local wavelength with a Gaussian profile. Although this is still somewhat arbitrary, the real physical picture will certainly be met better than without broadening. It should be noted that this focussing is a particular problem just with circular plasma cross-sections.

Figure 11 shows deposition profiles for electrons and protons at two different temperatures. In general, the widths of the profiles for the electrons are found to be quite similar to those of the protons, which might be affected to some extent by the numerical broadening. Particularly at higher temperatures the profiles are slightly peaked to the inside of the resonance layer.

Note that the calculations of the profiles do not include transport and losses of energy. The absolute peak values of the power density may be somewhat too large since a region of one local wavelength -as applied in our code for the broadening - is expected to be the minimum deposition width in a real experimental plasma. The influence of the plasma density and temperature profiles on the power deposition is illustrated in Fig. 12. No strong change of the deposition profiles and of the peak power densities is observed when the electron density and temperature profiles are changed from the rather peaked shapes, corresponding to the ohmic discharge phase (Fig. 13a), to the broader ones, related to the neutral beam-heated phase (Fig. 13b, c). This is to be expected since most variation of different plasma profiles occur in the plasma edge where absorption is negligible. Furthermore, the total power absorbed by electrons and ions does not change when varying the plasma profiles (Table 3), provided the central values of n_e , T_e , T_i are kept constant.

The relative flatness of the normalized plasma profiles (Fig. a-c) within $a/4$ explains why only weak changes of the absorbed power occur if the resonance layer for the second harmonic frequency $\omega = 2\Omega_{CH}$ is shifted somewhat out of axis (Fig. 14). It shows that the experiment should not be very sensitive to small deviations of the position of the resonance layer from the magnetic axis.

5. CONCLUSIONS

The results of the ray tracing approach appear to be reliable as far as transport and distribution of wave power and the scaling on electron density and plasma temperature are concerned while the evaluation of the power deposition profiles may involve some uncertainty.

In summary, ray tracing computations for ASDEX at $\omega = 2\Omega_{CH}$ predict substantial single transit absorption, particularly for neutral beam-preheated plasma conditions. The heating efficiency turns out to be already appreciable for ohmically heated plasmas and rapidly increases as the electron density and plasma temperature, reaching more than 40% single transit absorption at $T_{i0} = 3$ keV, $T_{e0} = 1.5$ keV, $n_{e0} = 5 \times 10^{13} \text{ cm}^{-3}$. Deposition profiles with peak power densities of a few W/cm^3 per MW are found to be well localized near the $\omega = 2\Omega_{CH}$ layer. They are rather insensitive to variations of the profiles for T_i , T_e and n_e . In the temperature range $T_{i0} \leq 3$ keV most of the power absorbed is taken by the plasma ions. The existence of a high-energy ion tail either generated by the rf itself or resulting from neutral beam injection may have a positive impact on the wave power absorption and the power distribution to ions and electrons [27, 28]. For this purpose a ray tracing code including a Fokker-Planck treatment of the high energy tail should be used.

6. APPENDIX

This section presents a complete set of plots obtained with the RAYIC code with fixed n_ϕ . Since it turns out that most absorption happens at the highest temperature - as to be expected - an example with the following parameters was chosen:

J_p	=	380 kA	f	=	70 MHz
$q(0)$	=	1.3	P_{rf}	=	1 MW
$q(a)$	=	3.1	n_ϕ	=	12

$$\begin{aligned}n_e(0) &= 5 \times 10^{13} \text{ cm}^{-3} \text{ (pure hydrogen)} \\T_e(0) &= 1.5 \text{ keV} \\T_i(0) &= 3.0 \text{ keV.}\end{aligned}$$

Figure A1 shows the normalized profiles of $n_e(r)$, $T_e(r)$, $T_i(r)$ and $q(r)$. The eight rays starting at different poloidal angles, and the corresponding wave fronts of the partial wave $n_\phi = 12$ are displayed in Fig. A2. For $n_\phi = 12$ and the plasma parameters listed above the whole power absorbed is transferred to the ions (see Fig. 10).

Figure A3 illustrates the refraction indices n_{perp} along the rays, where $S/2\pi$ is in units of local wave length. Typical values of n_{perp} at the plasma edge are about 20 to 25 increasing by a factor of about two in the

central plasma for rays starting near the torus midplane. The values of n_{perp} at various magnetic surfaces labeled by Ψ ($\Psi = r/a$ for circular plasmas) are plotted in Fig. A4. Owing to the poloidal symmetry of the eight ray starting points only four values of n_{perp} exist at the start, which then split into eight curves along the course in the plasma.

The dependence of n_x on Ψ is given in Fig. A5. Its variation over the plasma cross-section is typically $\pm 70\%$ with respect to the start values.

Figures A6 and A7 present the n_{\parallel} -variation along the ray paths through the plasma. n_{\parallel} increases by a factor of about 1.5 between the start and end points of the rays. The variation of n_z given in Fig. A8 is of the same order.

Figures A9 and A10 show the power transported by each ray versus $S/2\pi$ (in units of wave length) and Ψ , respectively. It is evident that most absorption occur within the resonance layer, which in this example is located at $S/2\pi \simeq 2.8$. The power deposition profile for the ions is given in Fig. A11. Since all power is transferred to the ions for $n_{\phi} = 12$, there is no profile of electron absorption.

REFERENCES

- /1/ HWANG,D., BITTER,M., BUDNY,R. et al., Proc. 9th Internat. Conf. on Plasma Physics and Controlled Nuclear Fusion Research, Baltimore (1982), Vol. 2, 3 (1983)
- /2/ ADAM,J., Plasma Physics and Controlled Fusion 25 (1A), 165 (1984)
- /3/ ODAJIMA,K., MATSUMOTO,H., KIMURA,H. et al., Proc. 4th Internat. Symp. on Heating in Toroidal Plasmas, Rome (1984)
- /4/ MATSUMOTO,M., KIMURA,H., ODAJIMA,K. et al., Nucl. Fusion 24 (3), 283 (1984)
- /5/ WESNER,F., BRAUN,F., FRITSCH,R. et al., Proc. 3rd Internat. Symp. on Heating in Toroidal Plasmas, Grenoble, Vol. I, 429 (1982)
- /6/ WESNER,F., BRAUN,F., FRITSCH,R. et al., Proc 4th Internat. Symp. on Heating in Toroidal Plasmas, Rome (1984)
- /7/ STIX,T.H., Nucl. Fusion 15, 737 (1975)
- /8/ SWANSON,D.G., Phys.Rev.Lett. 36,316 (1976)
- /9/ SWANSON,D.G., Proc. 3rd Intern. Symp. on Heating in Toroidal Plasmas, Grenoble, Vol. I, 285 (1982)
- /10/ SWANSON,D.G., Nucl. Fusion 20, 949 (1980)
- /11/ JAQUINOT,J., McVEY,B.D., SCHARER,J.E., Phys.Rev.Lett. 39, 88 (1977)
- /12/ PERKINS,F.W., Nucl. Fusion 17, 1197 (1977)
- /13/ COLESTOCK,P.L., KASHUBA,R.J., Nucl. Fusion 23, 763 (1983)
- /14/ CHIU,S.C., MAU,T.K., Nucl.Fusion 23,1613 (1983)
- /15/ ITOH,K., ITOH,S.-I., FUKUYAMA,A., Nucl. Fusion 24, 13 (1984)
- /16/ BRAMBILLA,M., Report IPP 4/210, Max-Planck-Institut für Plasmaphysik, Garching(1983)
- /17/ BRAMBILLA,M., OTTAVIANI,M., Report IPP 4/212, Max-Planck-Institut für Plasmaphysik, Garching(1983)
- /18/ BHATNAGAR,V.P. et al., Rep. No. 81, Ecole Royale Militaire, Brussels(1983)
- /19/ HWANG,D.Q. et al., Proc. 5th Topical Conf. on Radio Frequency Plasma Heating, Madison(1983)
- /20/ BRAMBILLA,M., Report IPP 4/217, Max-Planck-Institut für Plasmaphysik, Garching(1984)

- /21/ BRAMBILLA,M., Report IPP 4/216/, MPI für Plasmaphysik, Garching(1984)
- /22/ WEYNANTS,R.R., Proc. 4th Internat.Symp. on Heating in Toroidal Plasmas, Rome (1984)
- /23/ SÖLL,M., SPRINGMANN,E., Report IPP, to be published, Max-Planck-Institut für Plasmaphysik, Garching(1984)
- /24/ SÖLL,M., WESNER,F., Proc. 10th Symp. on Fusion Engineering, Philadelphia, 2P20 (1983)
- /25/ WEYNANTS,R.R., Phys.Rev.Lett. 33, 78 (1974)
- /26/ BRAMBILLA,M., Report IPP 4/209, MPI für Plasmaphysik, Garching(1982)
- /27/ HWANG,D.Q., KARNEY,C.F.F., HOSEA,J.C. et al., Report PPPL-1990, Princeton (1983)
- /28/ ITOH, S.-I., FUKUYAMA,A., ITOH,K., Nucl.Fusion 24, 224 (1984)

A N T E N N A D A T A

distance antenna-plasma	:	7 cm
distance antenna-wall	:	6 cm
width of antenna element	:	18 cm
length of antenna element	:	39 cm
number of antenna elements	:	4
phase difference	:	0

Table 1

P L A S M A D A T A

circular hydrogen plasma

major radius	:	165 cm
minor radius	:	40 cm
toroidal magnetic field	:	2.30 T
plasma current	:	250 to 450 kA
central electron density	:	3 to 7.10 ¹³ cm ⁻³
edge density	:	a few 10 ¹² cm ⁻³
central electron temperature:		0.7 to 1.5 keV
central ion temperature	:	0.5 to 3.0 keV

Table 2

	P_e [kW]	P_{H^+} [kW]	P_{abs} [kW]
OH-profiles	66	261	327
L-profiles	66	264	330
H-profiles	66	275	341

$(T_{eo} = 0.8 \text{ keV}, T_{io} = 1.5 \text{ keV}, n_{eo} = 5.10^{13} \text{ cm}^{-3},$
 $P_{rf} = 1 \text{ MW})$

Table 3

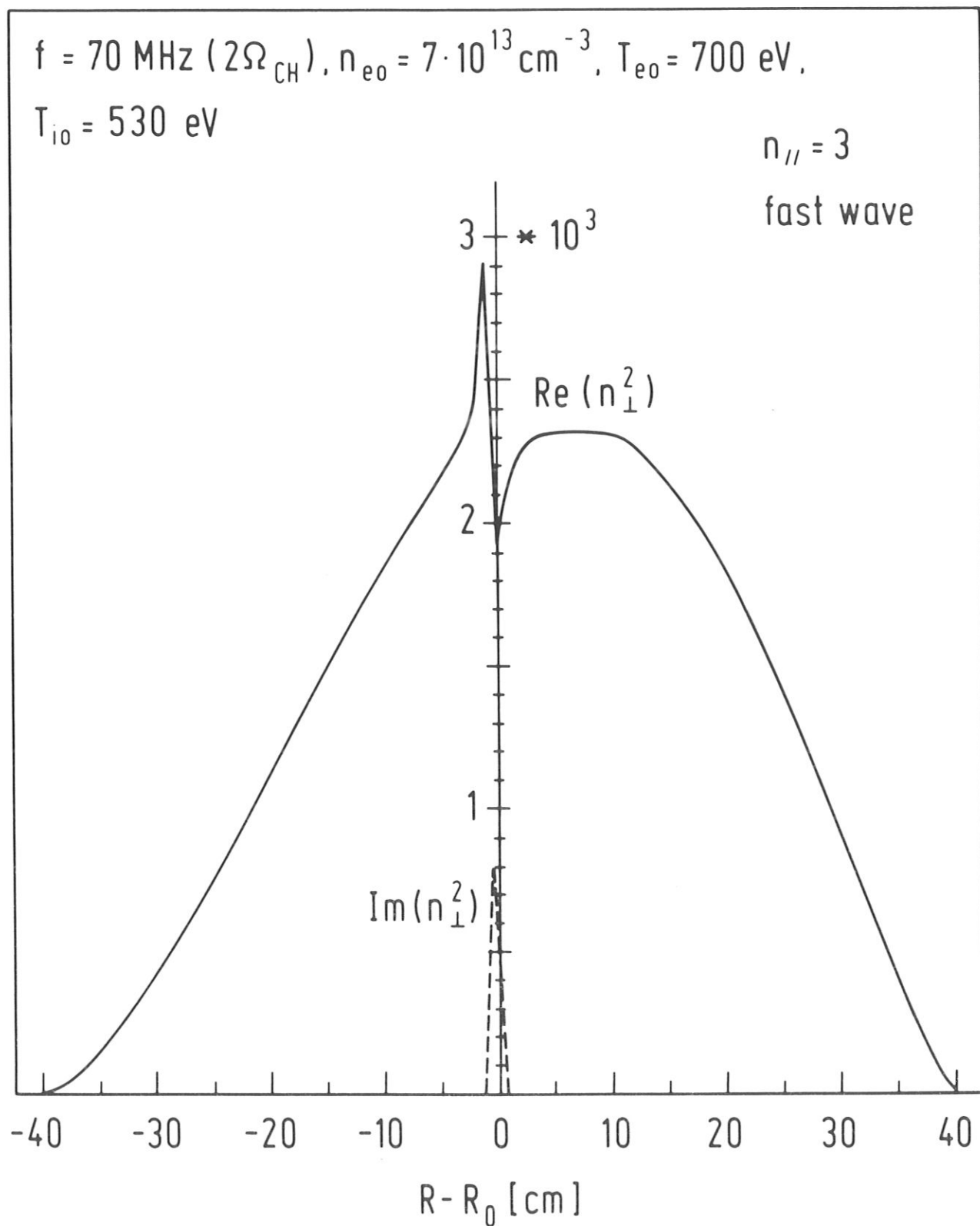


Fig.1: Dependence of n_{\perp}^2 on plasma radius (R_0 denotes the major radius, $R_0 = 165 \text{ cm}$).

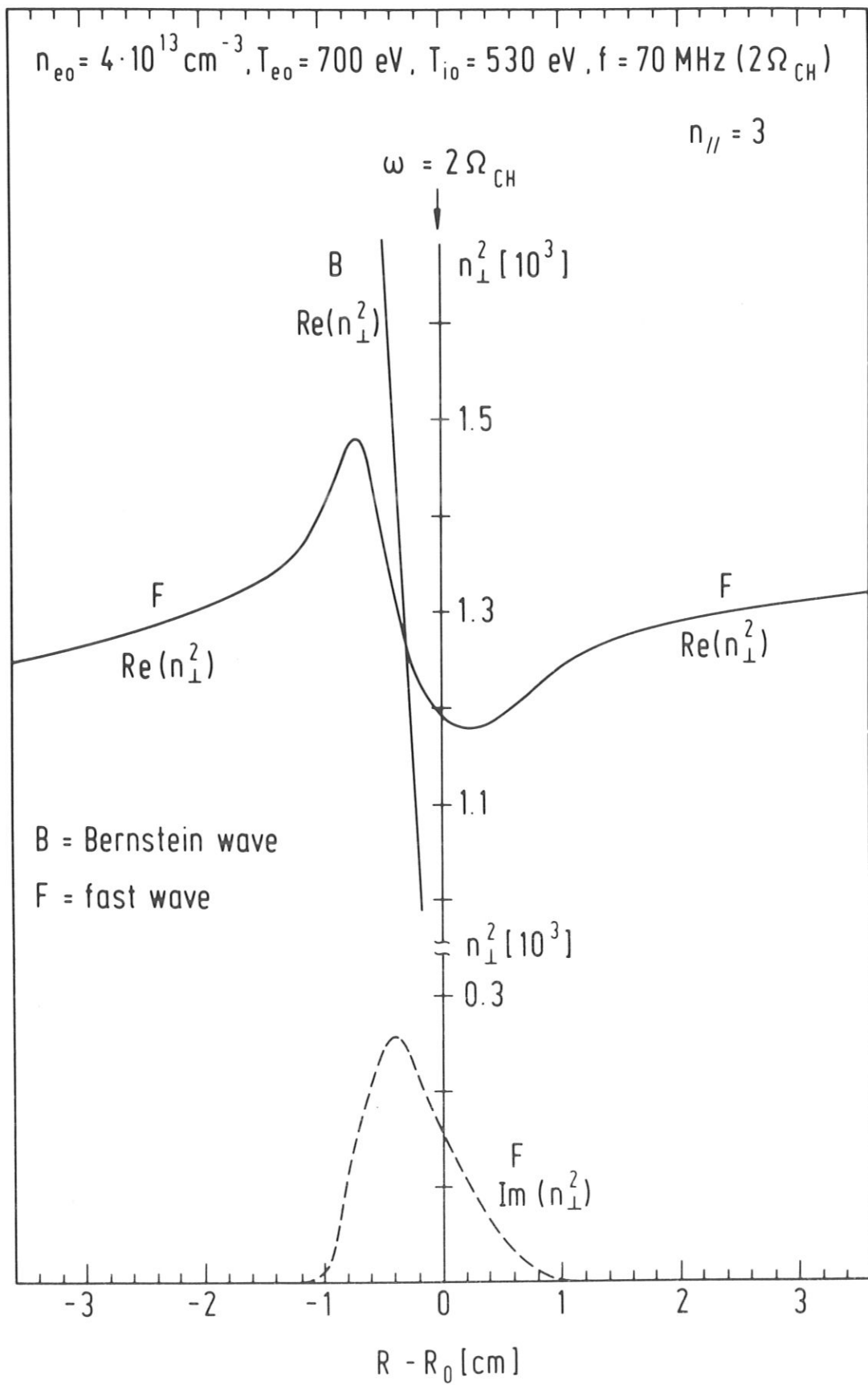


Fig.2: Dependence of perpendicular refractive index on radius near the resonance layer.

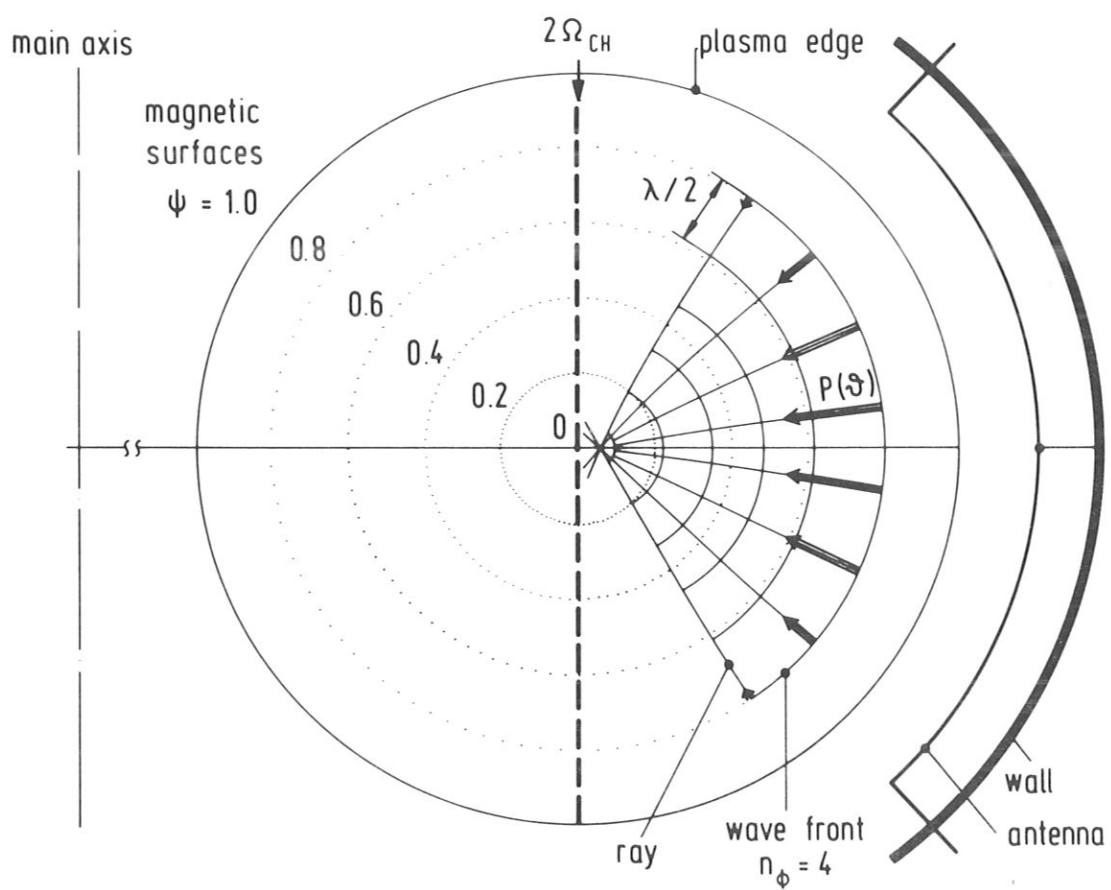


Fig.3: Poloidal cross-section of the plasma with magnetic surfaces, the position of one double-antenna, and the evolution of wave fronts for $n_\phi = 4$.

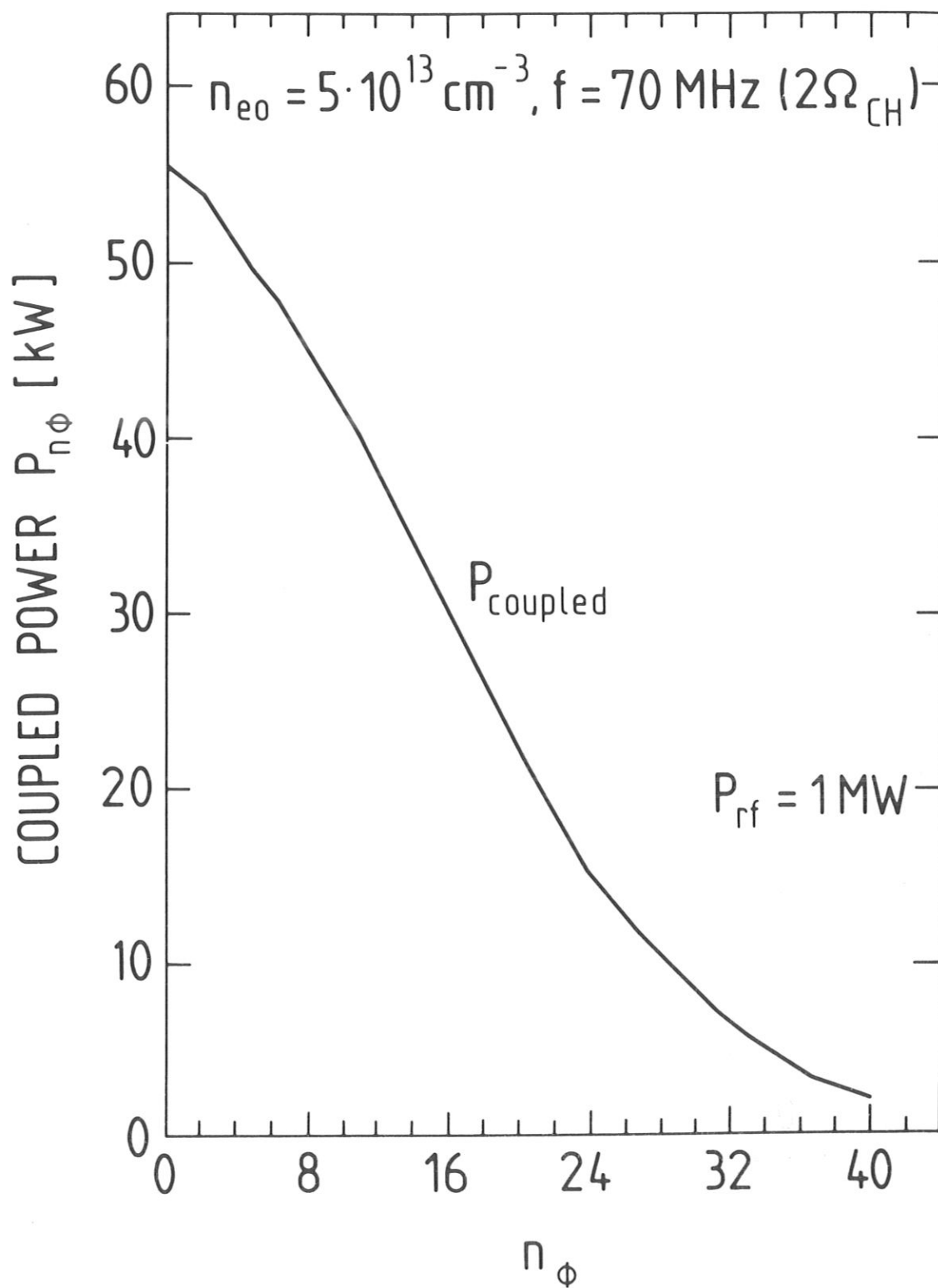


Fig.4: Power spectrum of partial waves radiated by an ASDEX-like double antenna.

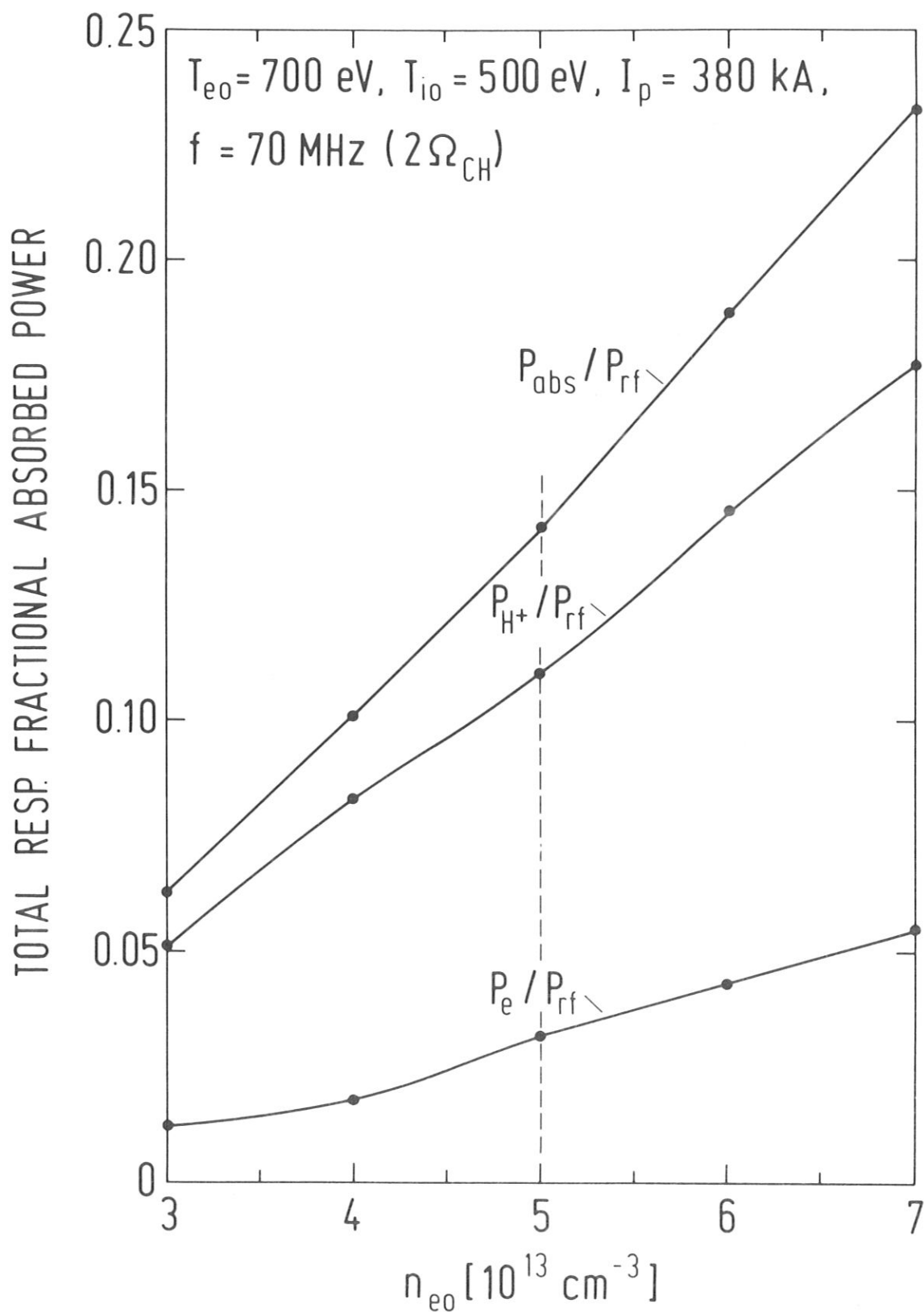


Fig.5: Dependence of fractional and total absorbed power on electron density (P_e , P_{H^+} denote the fraction of power taken by the electrons and ions respectively, $P_{abs} = P_e + P_{H^+}$).

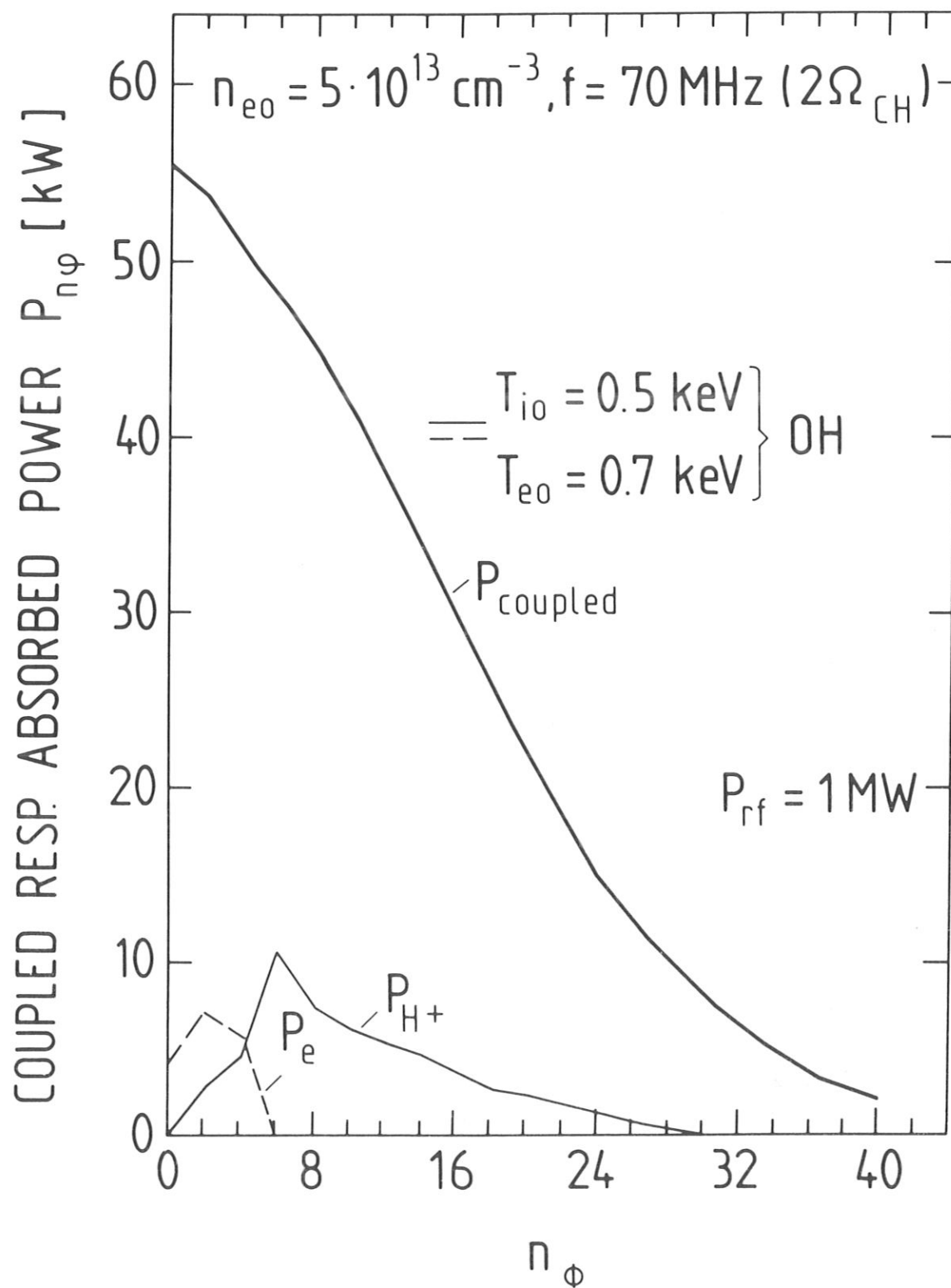


Fig.6: Absorbed power distributions of partial waves for electrons and ions (ohmic discharge conditions).

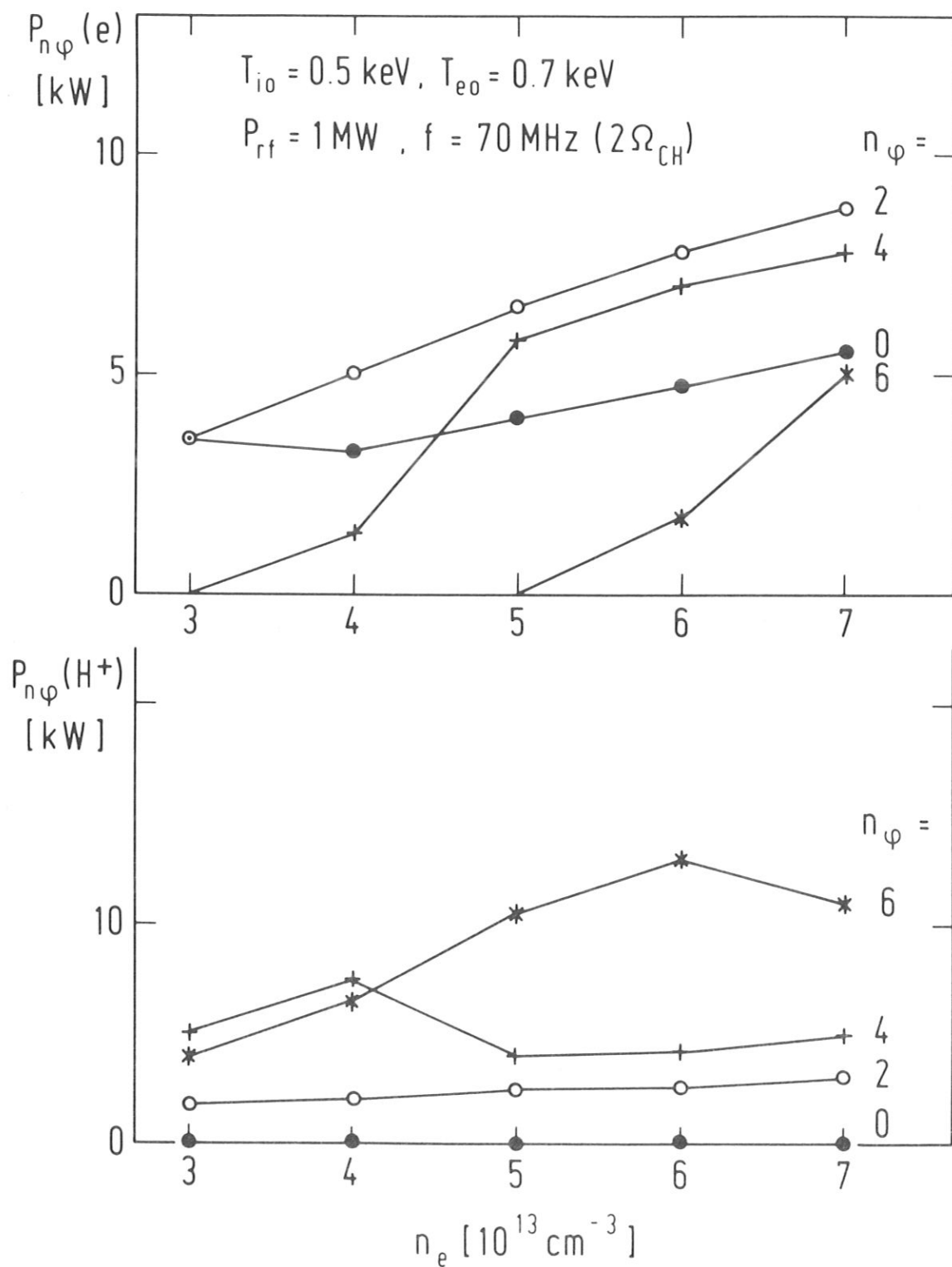


Fig.7: Power absorption of various partial waves versus electron peak density.

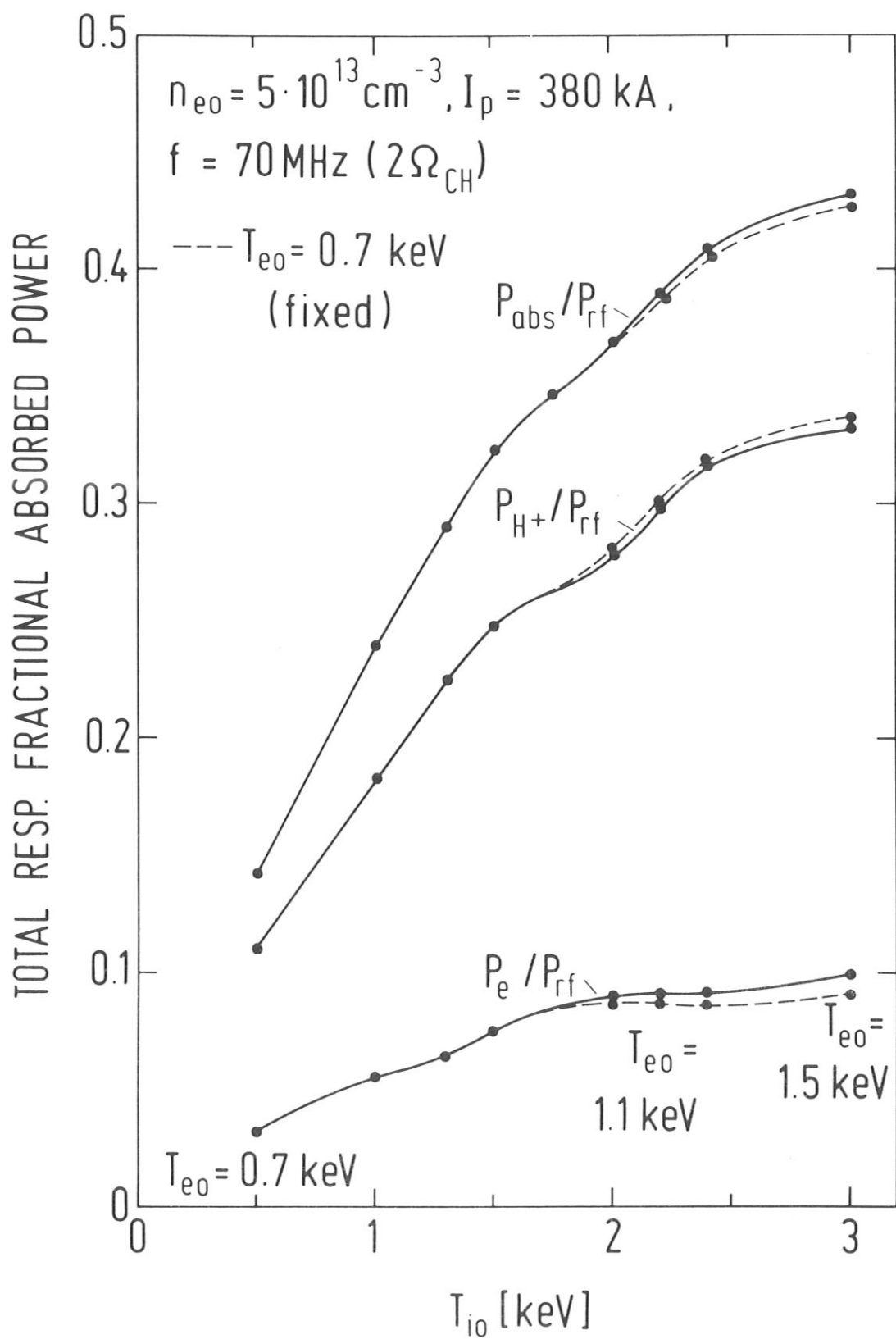


Fig.8:

Fractional and totally absorbed power versus central ion temperature for fixed T_{e0} (dashed lines) and floating T_{e0} (solid lines).

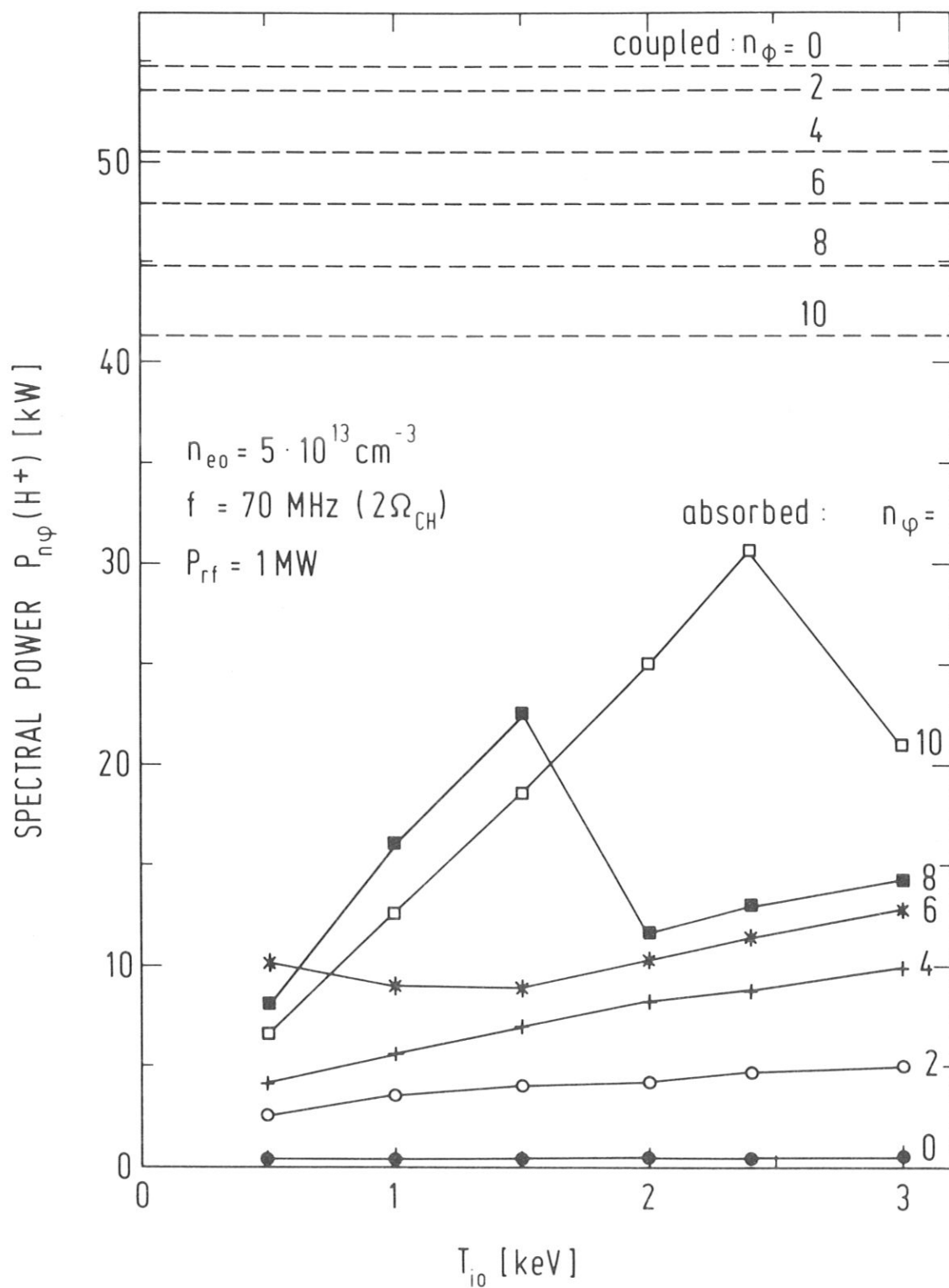


Fig.9: Spectral power distribution for various partial waves versus central ion temperature.

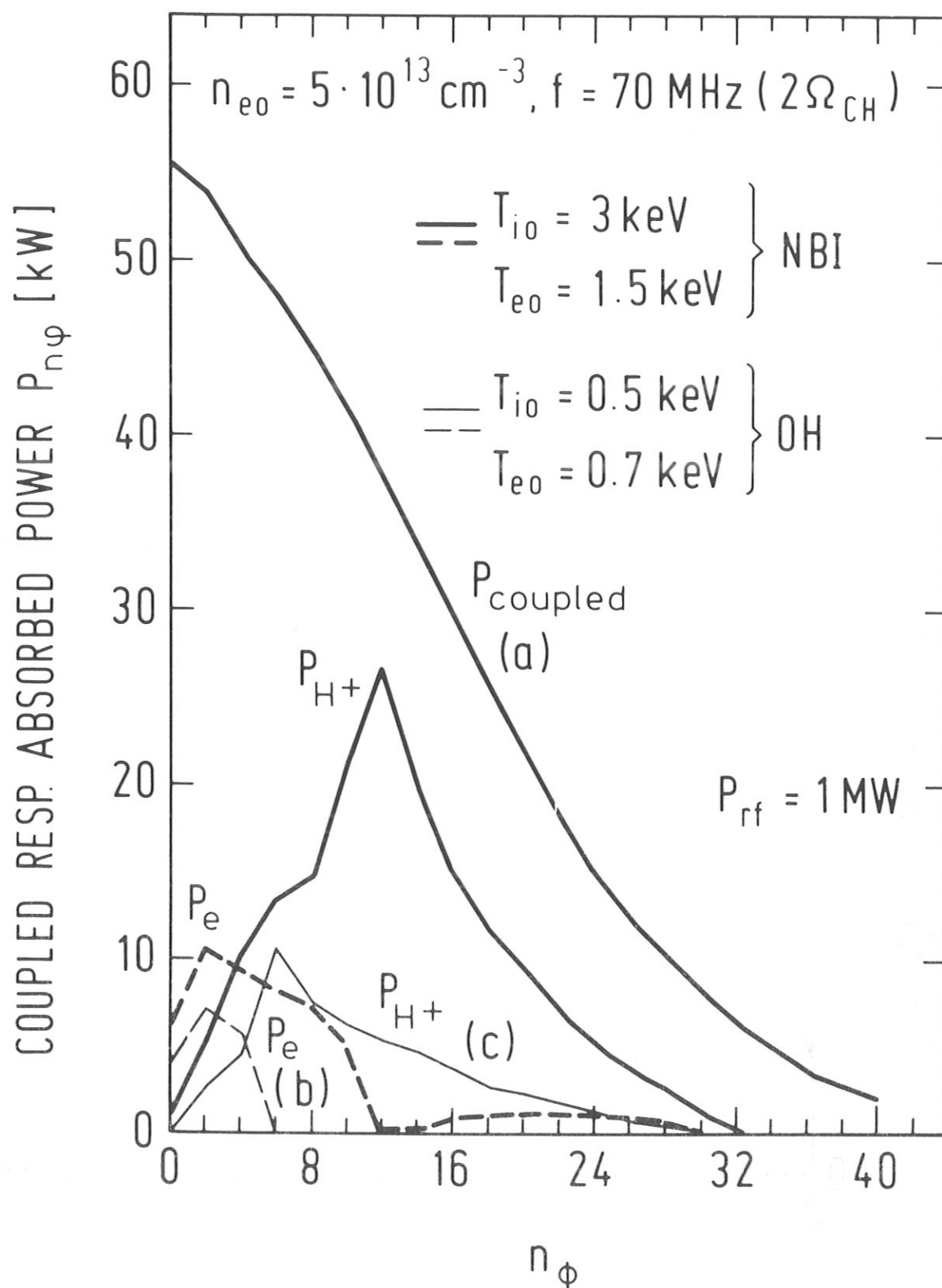


Fig.10: Coupled and absorbed power spectra for different target plasma temperatures.

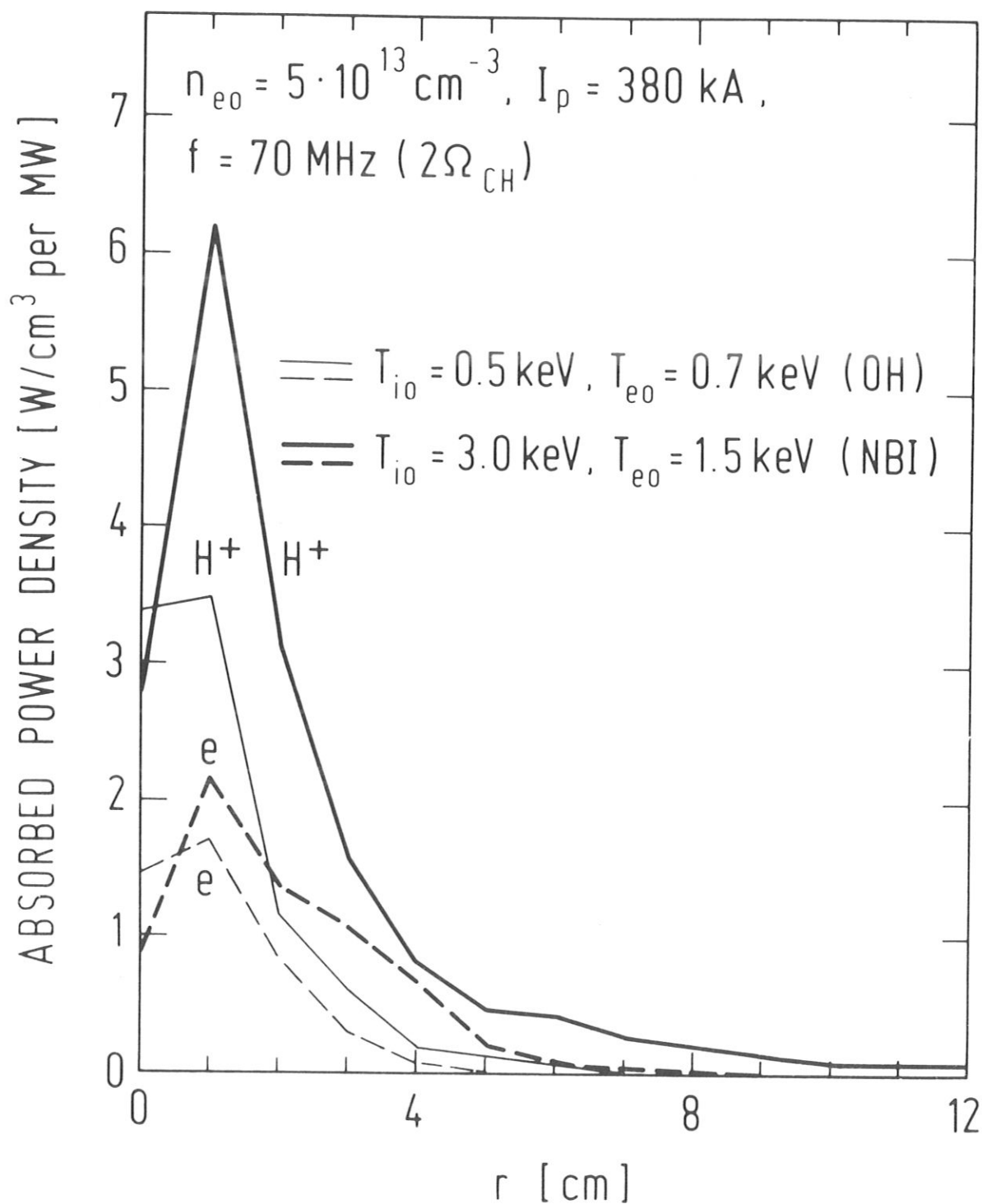


Fig.11: Power deposition profiles at two different plasma temperatures.

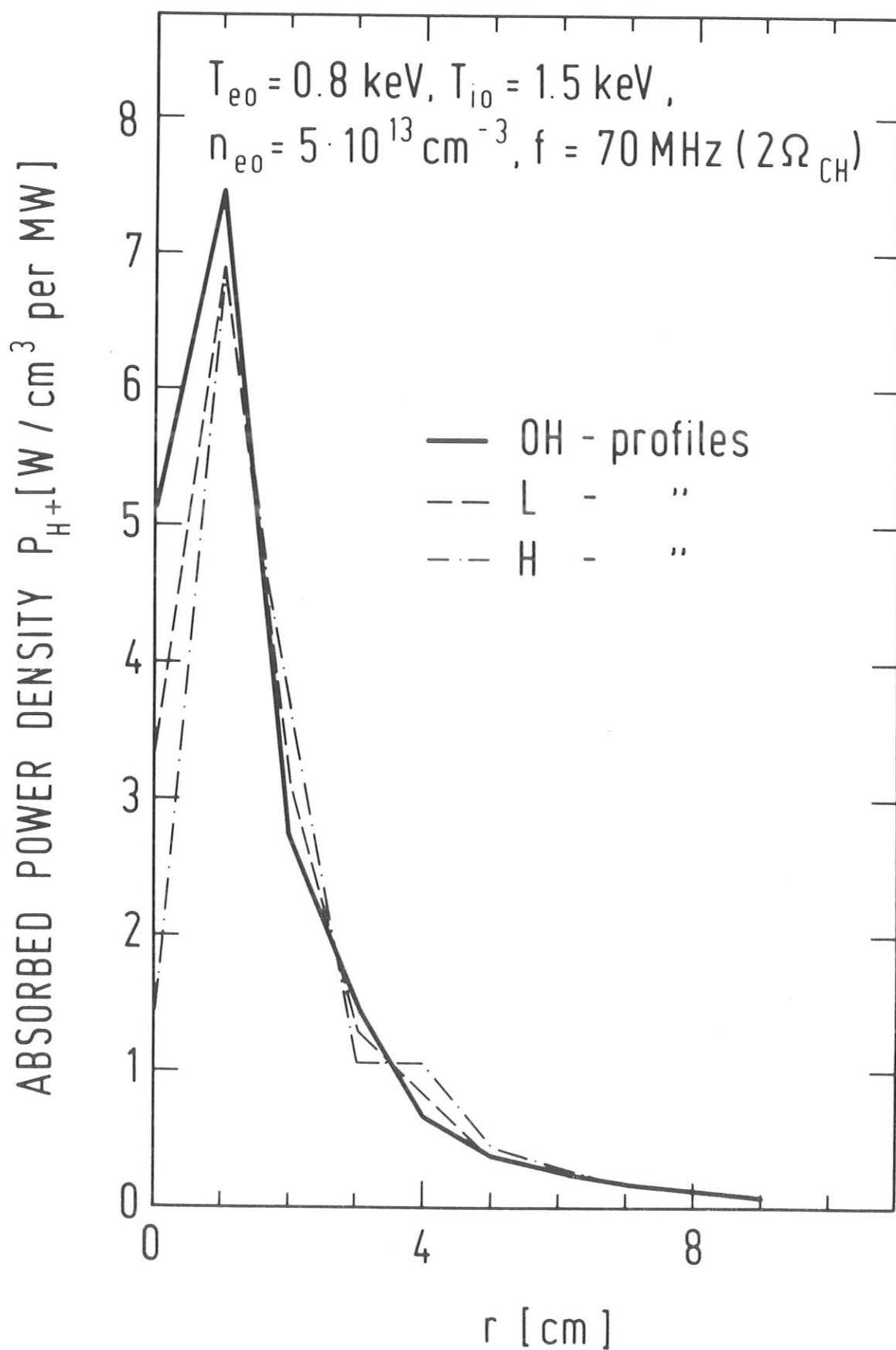


Fig.12: Influence of different plasma temperature and density profiles on the power deposition profile for ions.

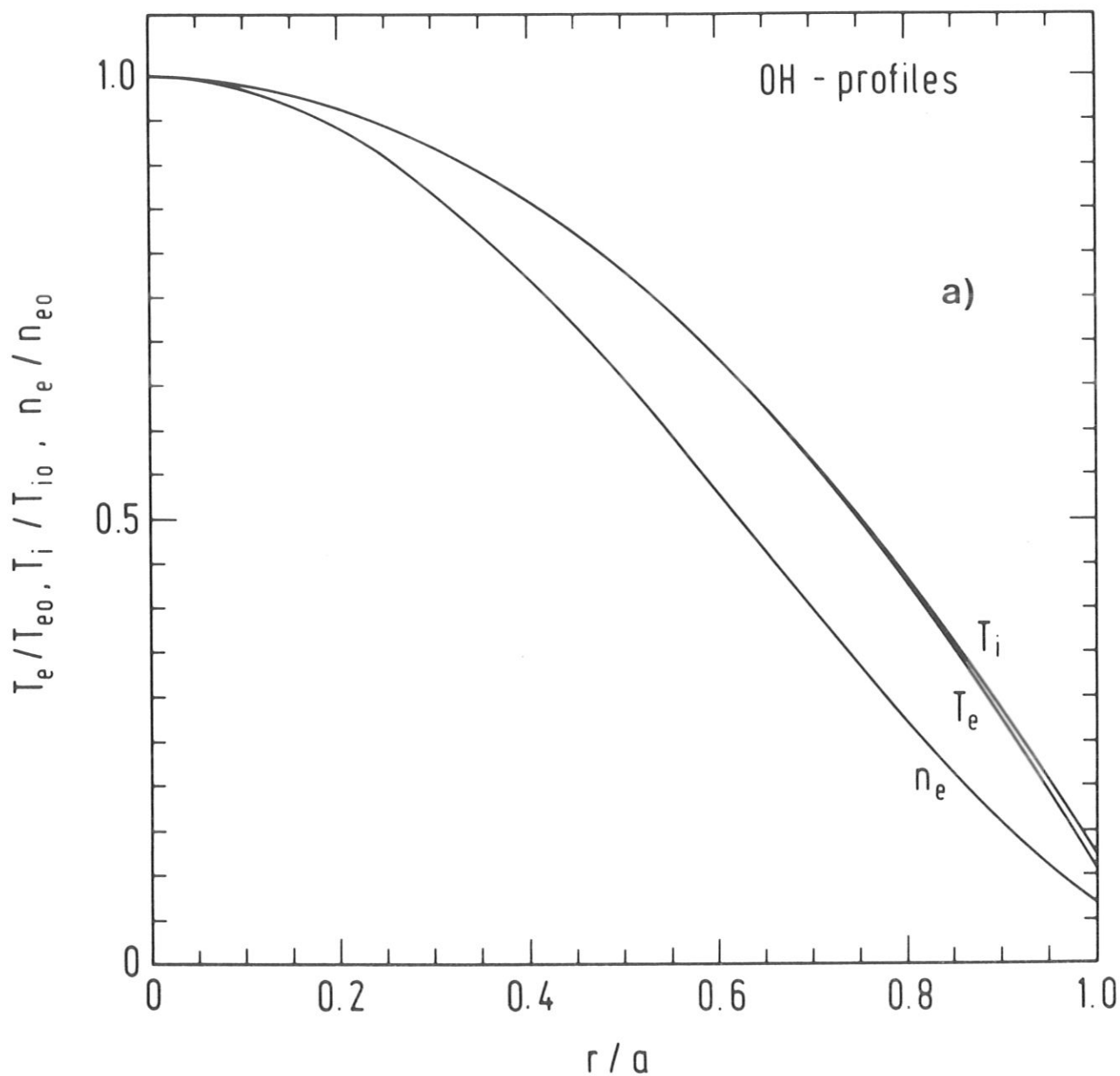


Fig.13: Profiles of electron density, electron and ion temperature as applied to simulate
a) ohmic discharge phase
b) L-type neutral beam injection phase
c) H-type neutral beam injection phase.

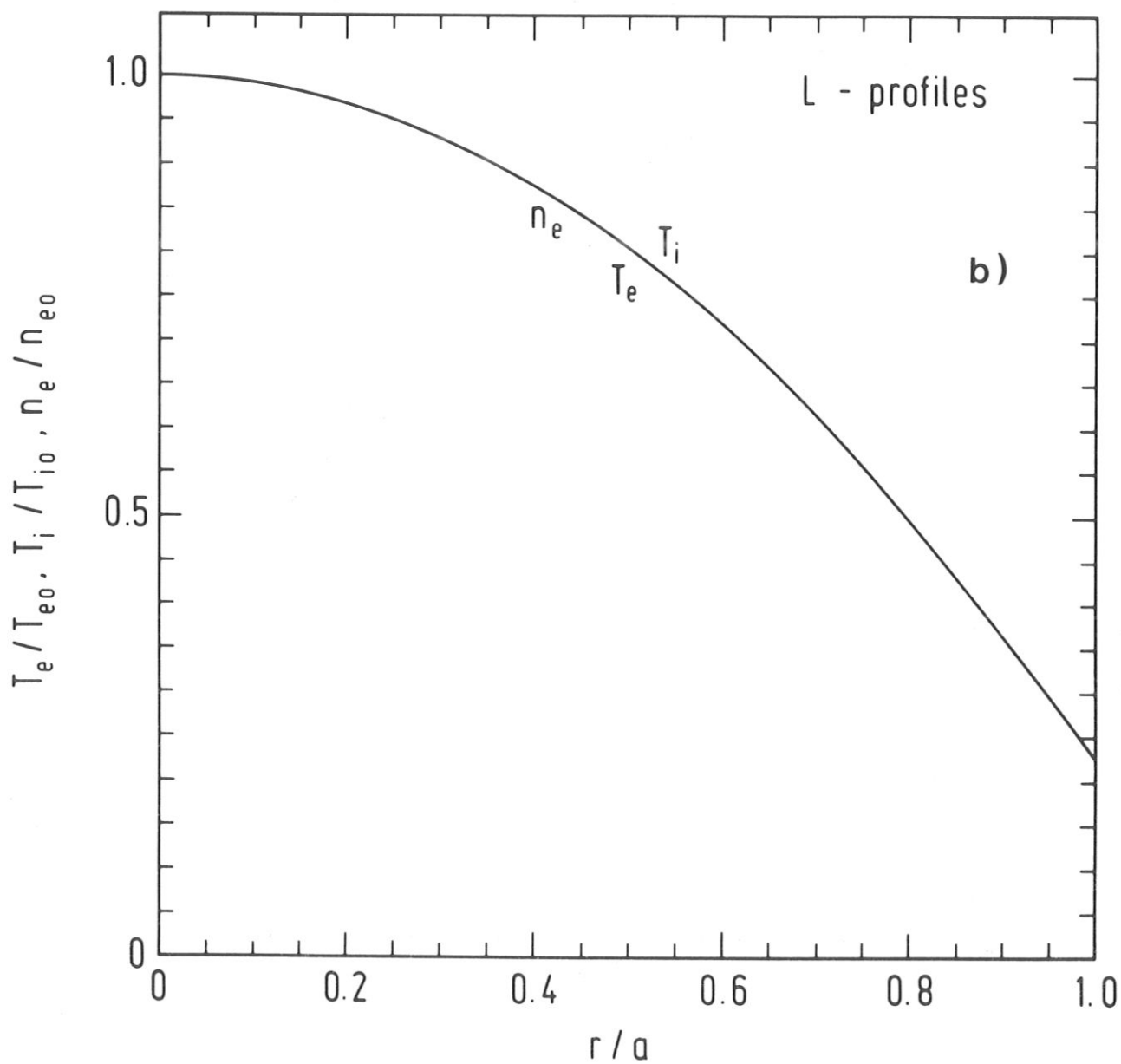


Fig. 13 b

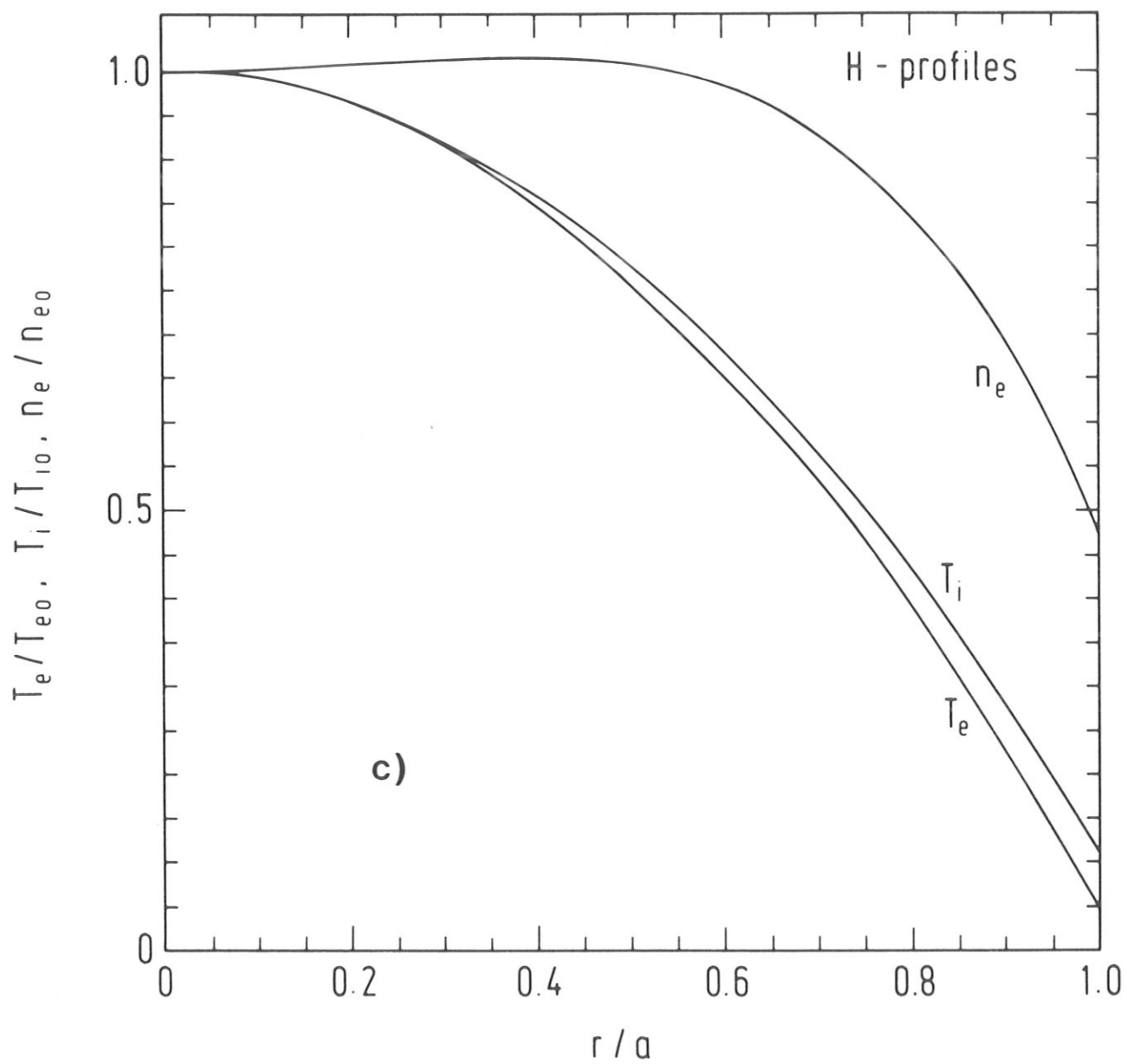


Fig. 13 c

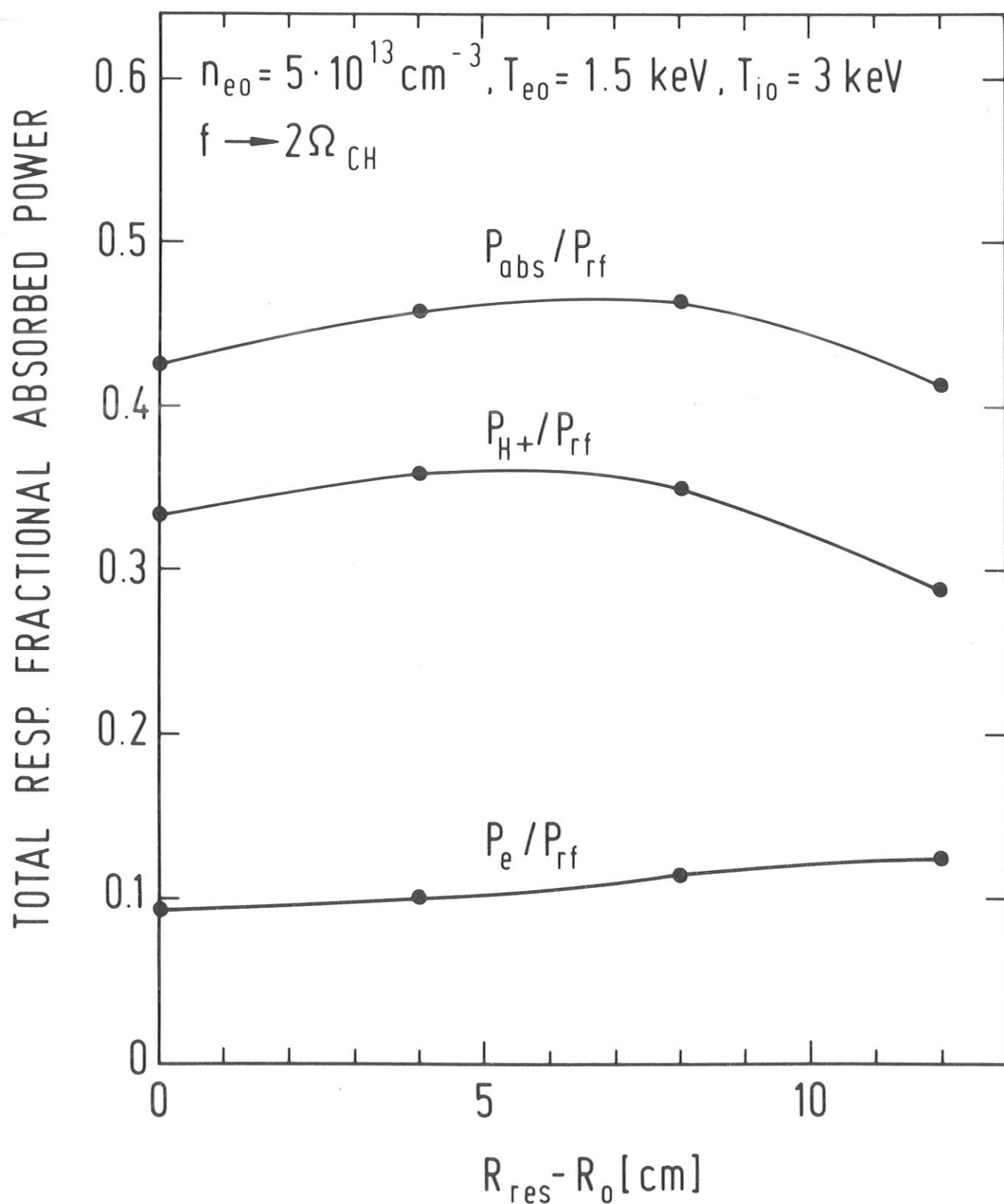


Fig.14: Fractional and totally absorbed power versus the shift of the resonance layer from the magnetic (plasma) axis.

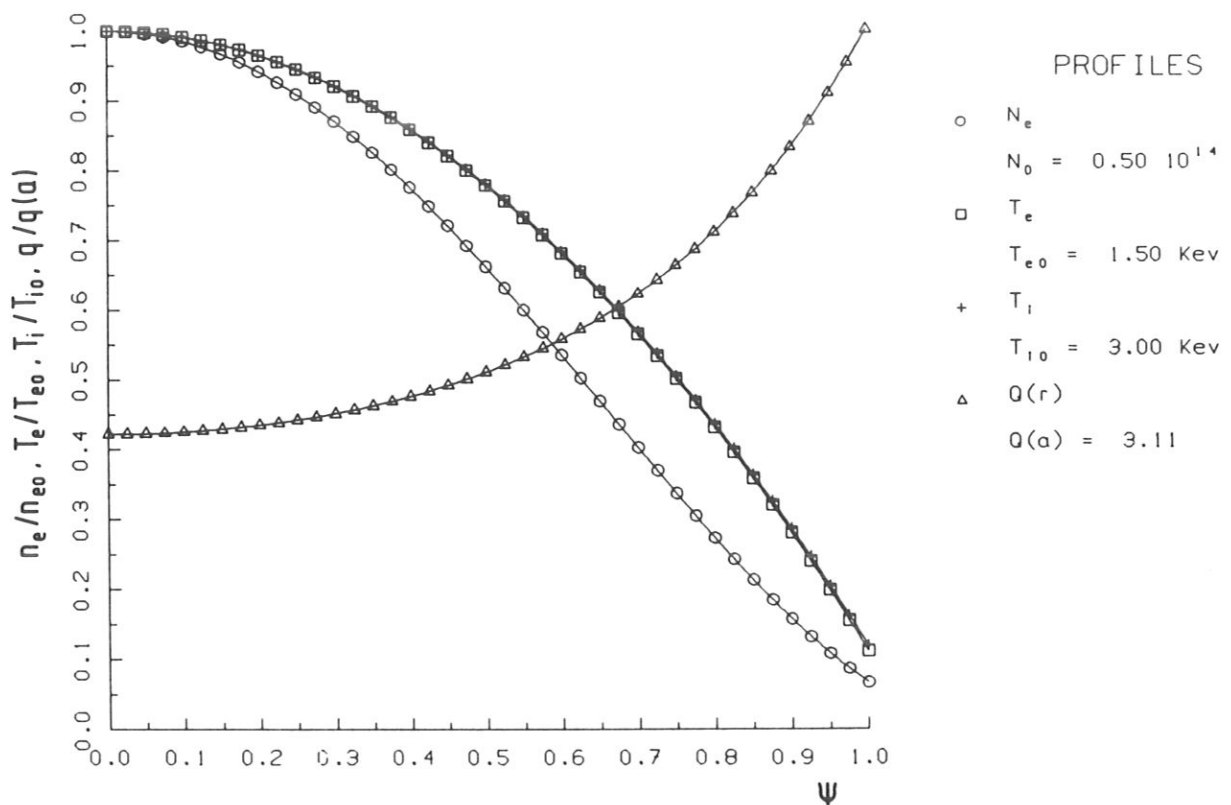


Fig.A1: Profile plots of n_e , T_e , T_i and q .

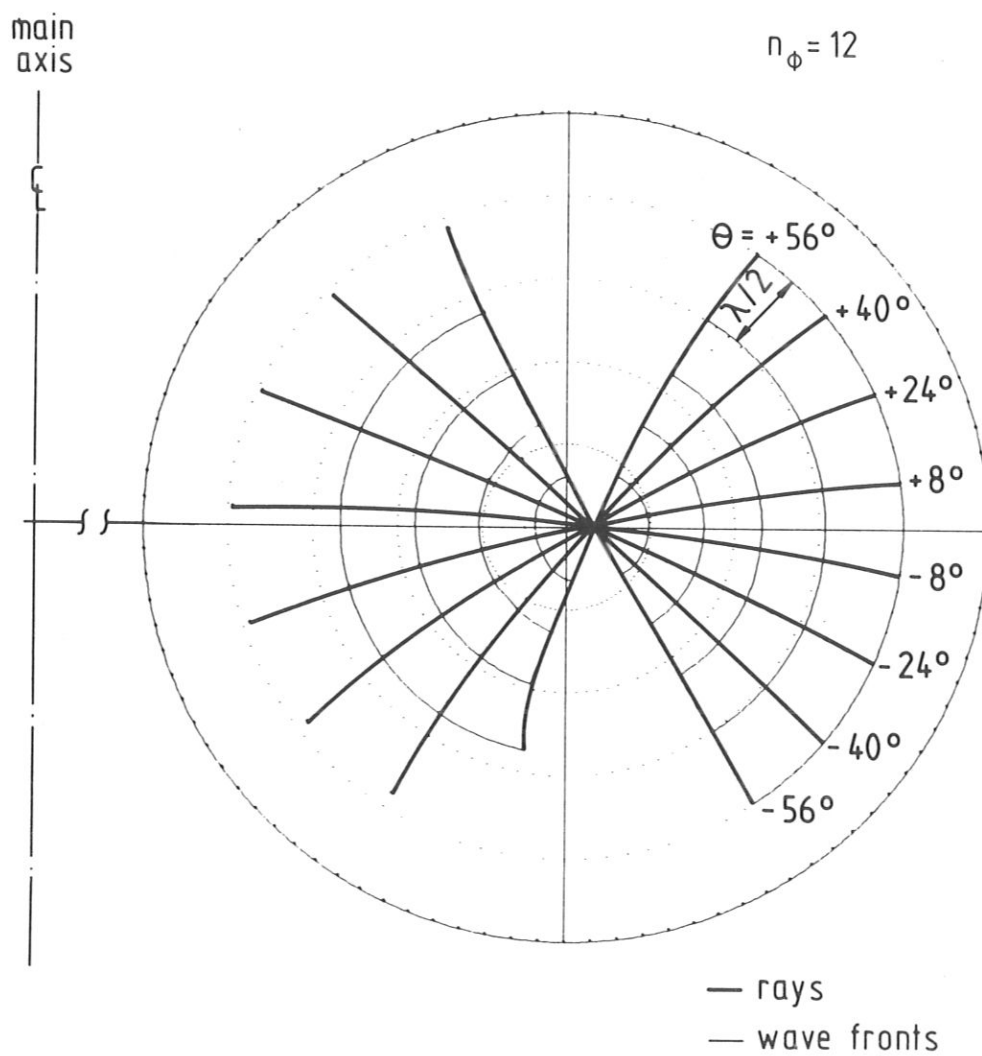


Fig.A2: Poloidal plasma cross-section and distribution of rays for $n_\phi = 12$.

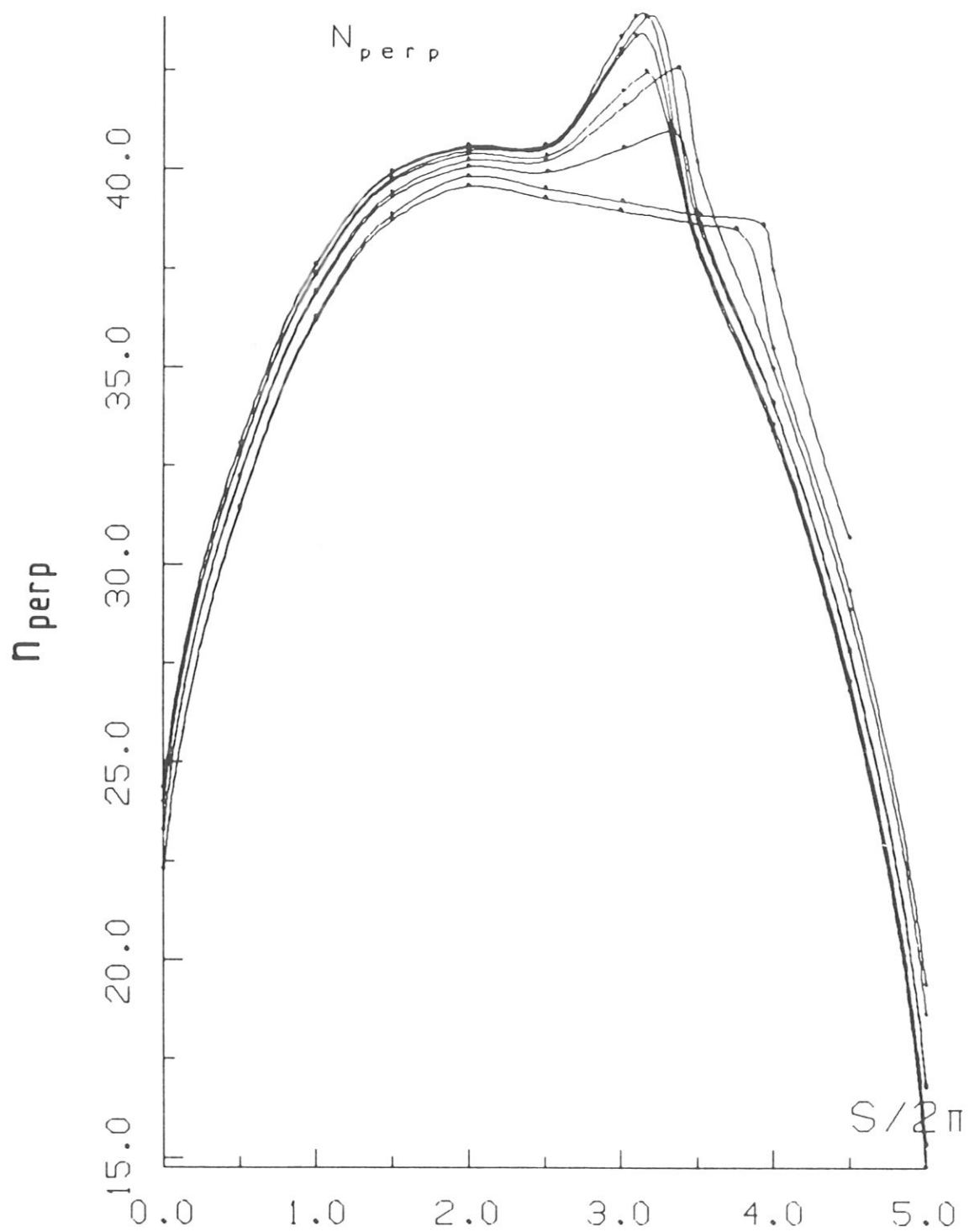


Fig.A3: n_{perp} versus $S/2\pi$ (in units of local wave lengths).

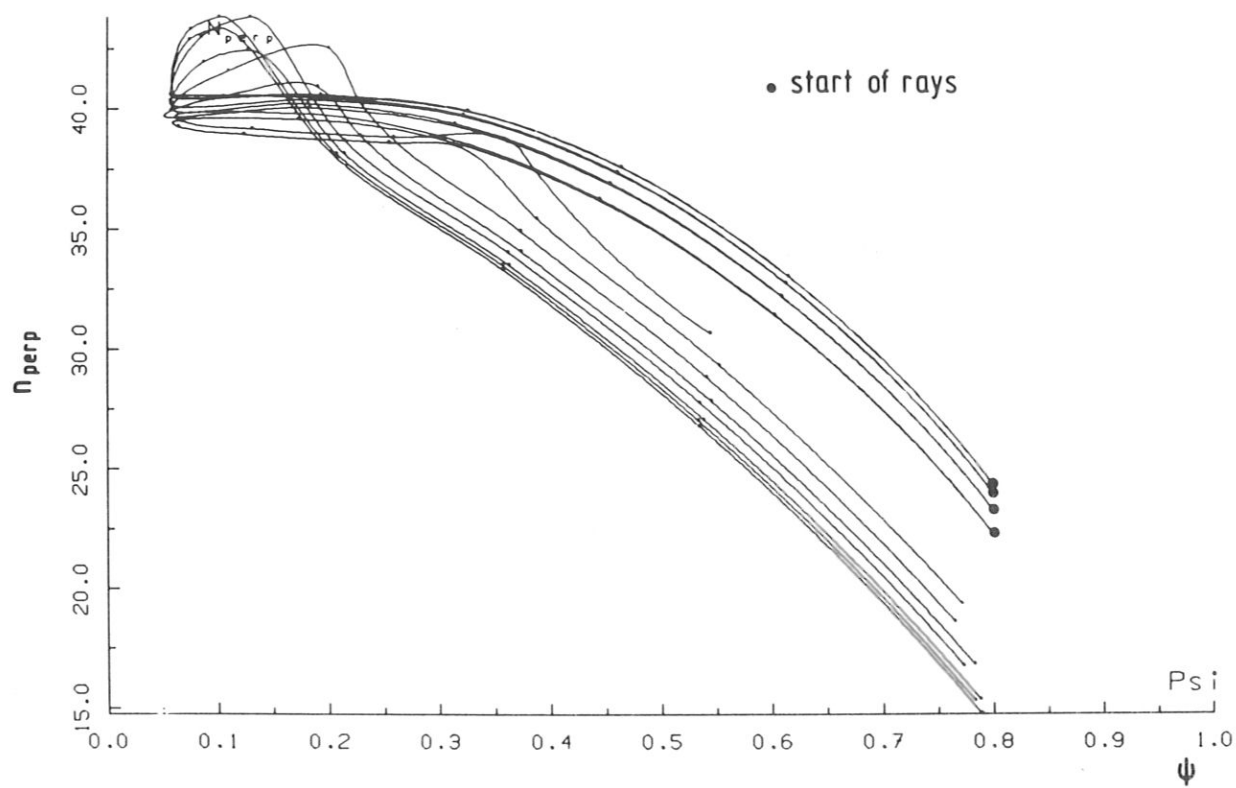


Fig.A4: n_{perp} versus radii of magnetic surfaces.

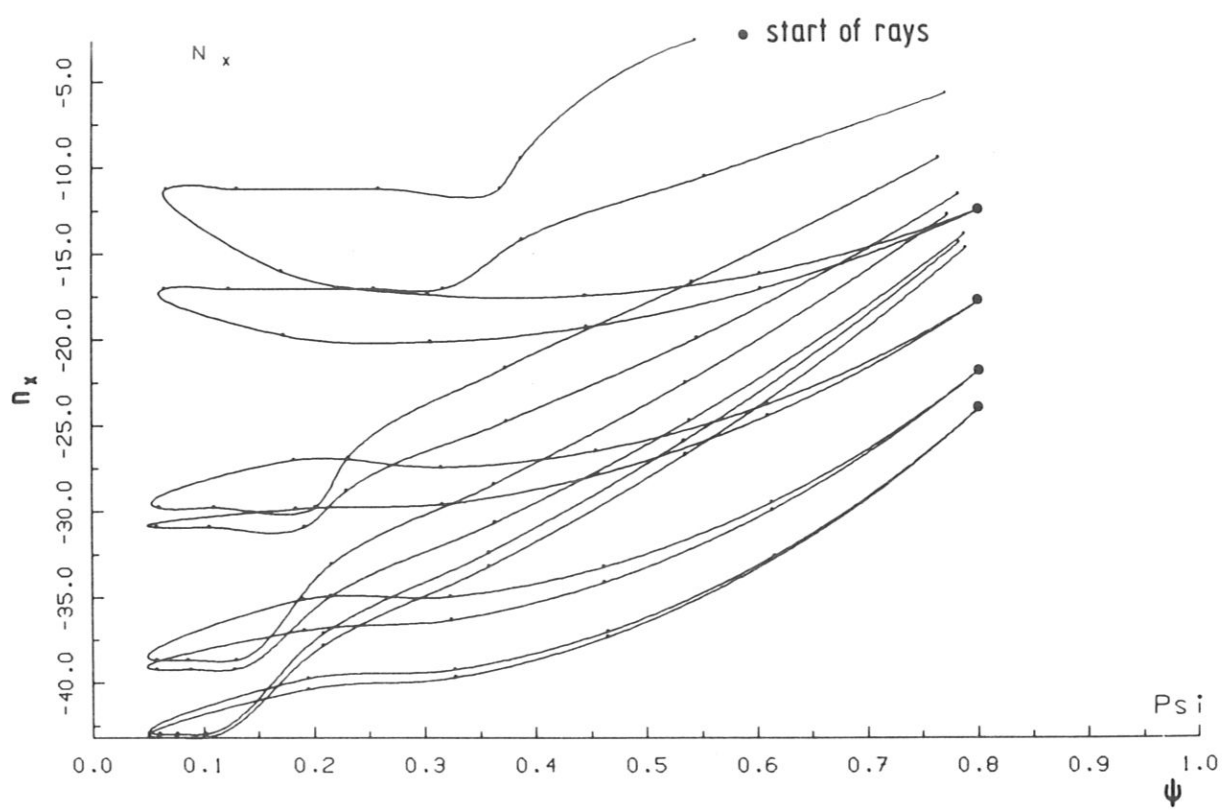


Fig.A5: n_x versus radii of magnetic surfaces.

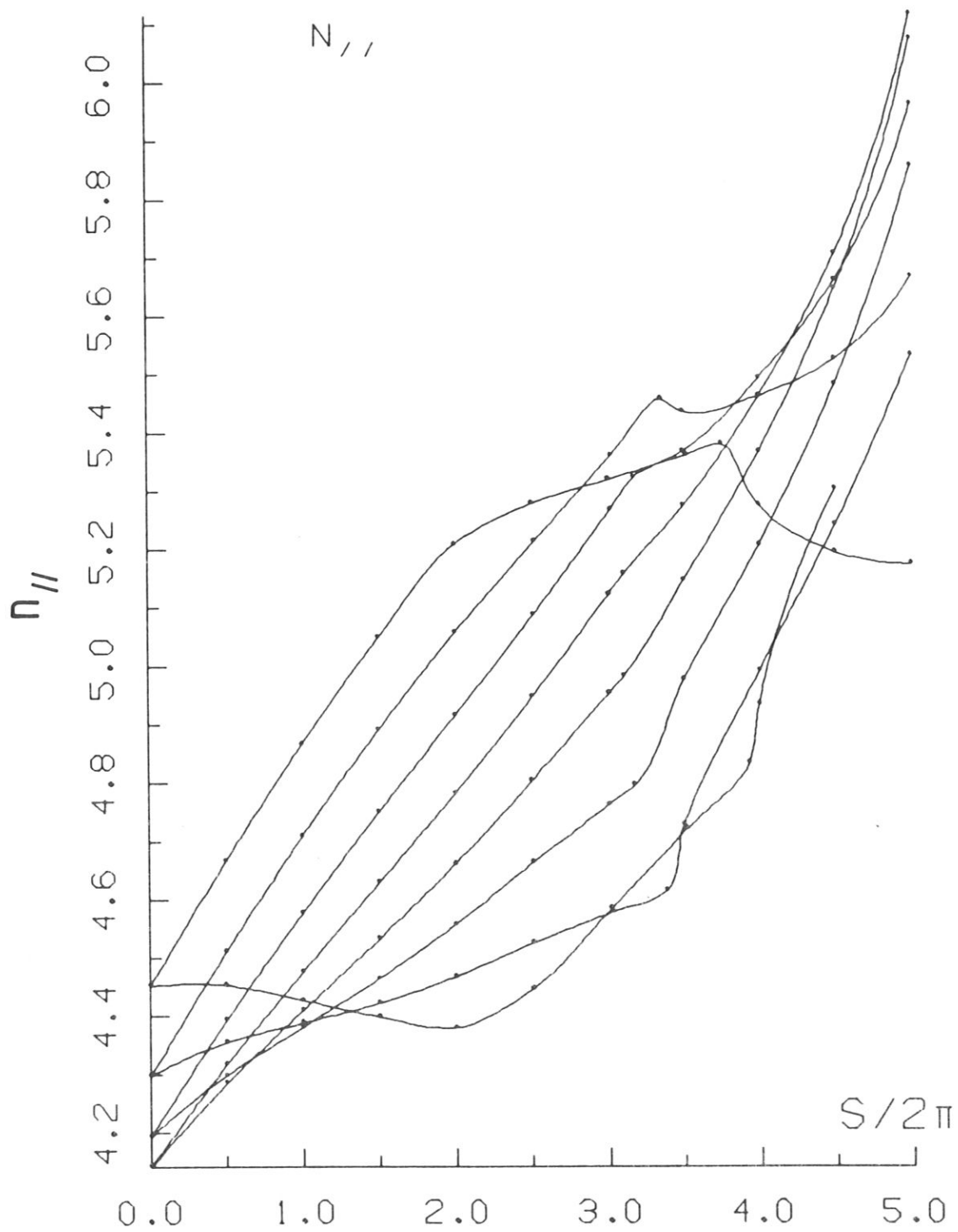


Fig.A6: $n_{//}$ versus $S/2\pi$.

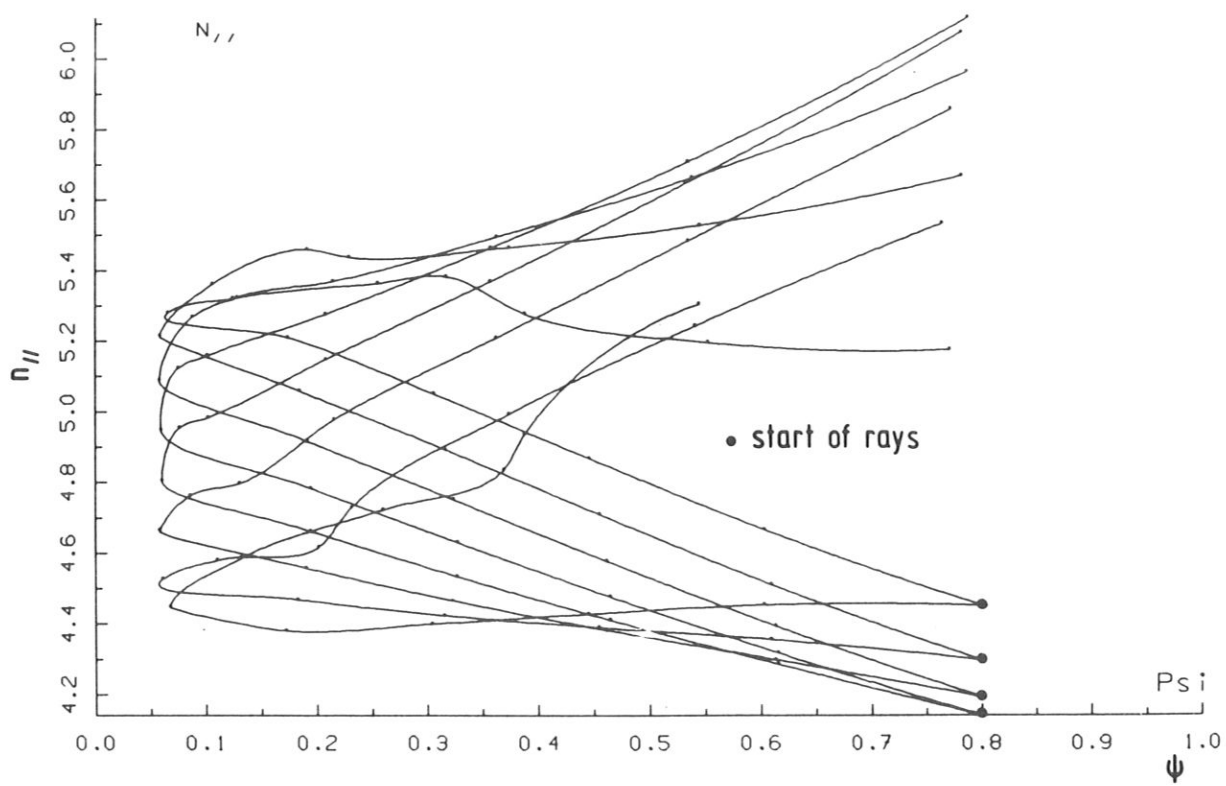


Fig.A7: $n_{||}$ versus ψ .

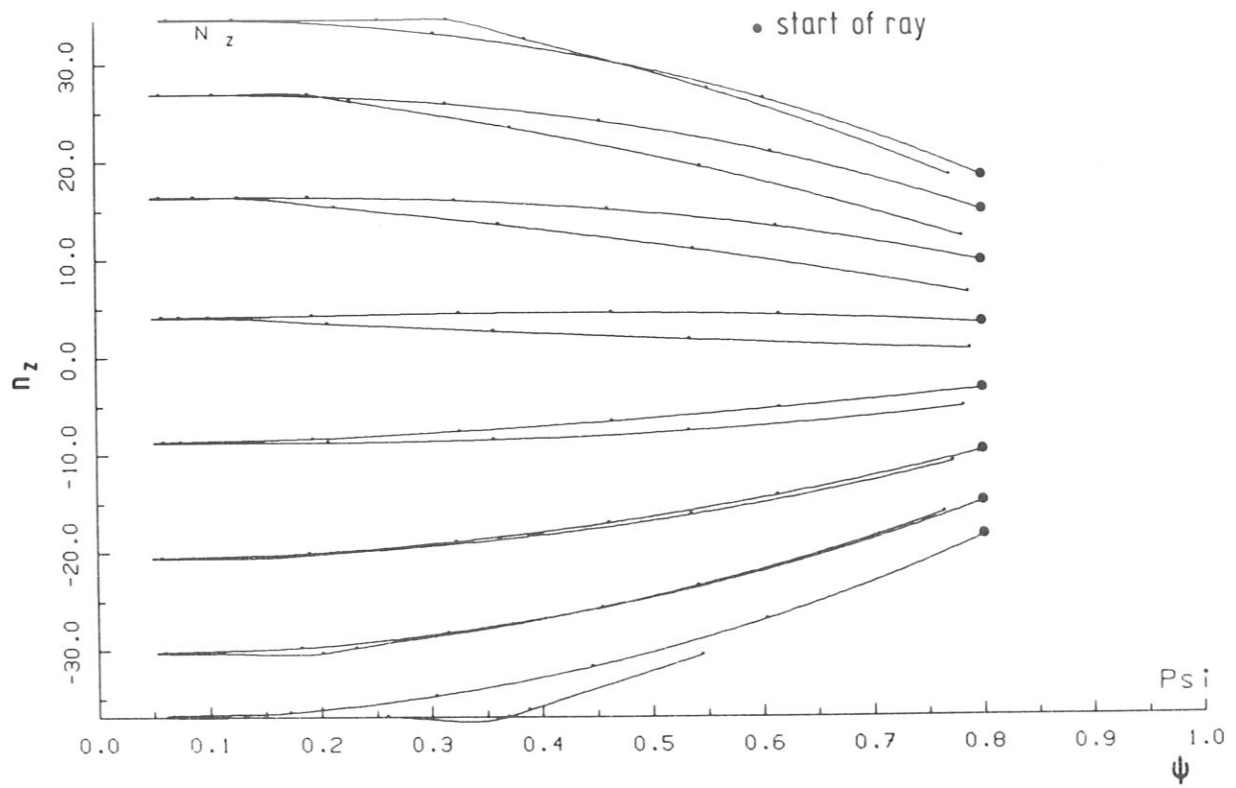


Fig.A8: n_z versus ψ .

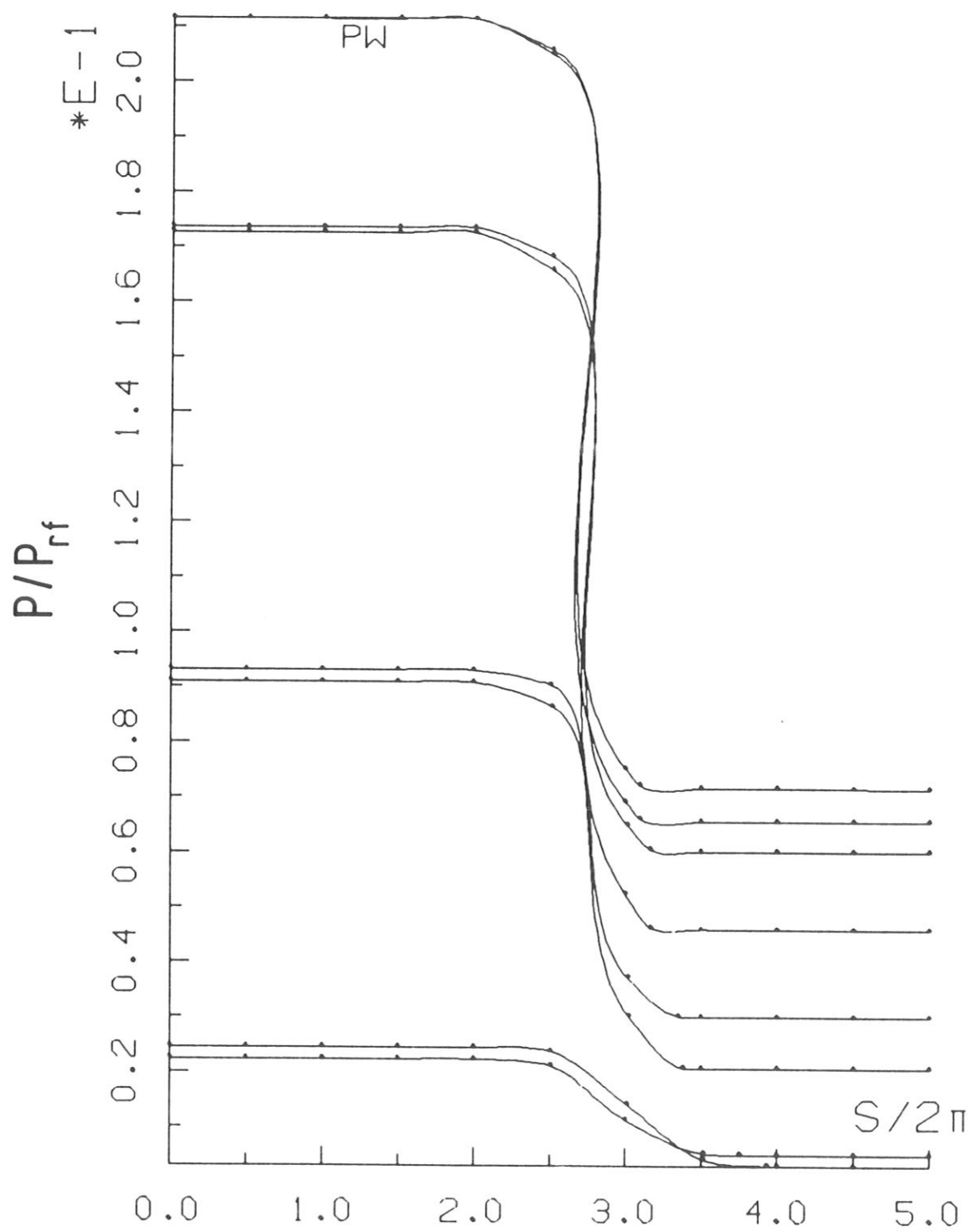


Fig.A9: Transported power along each ray path.

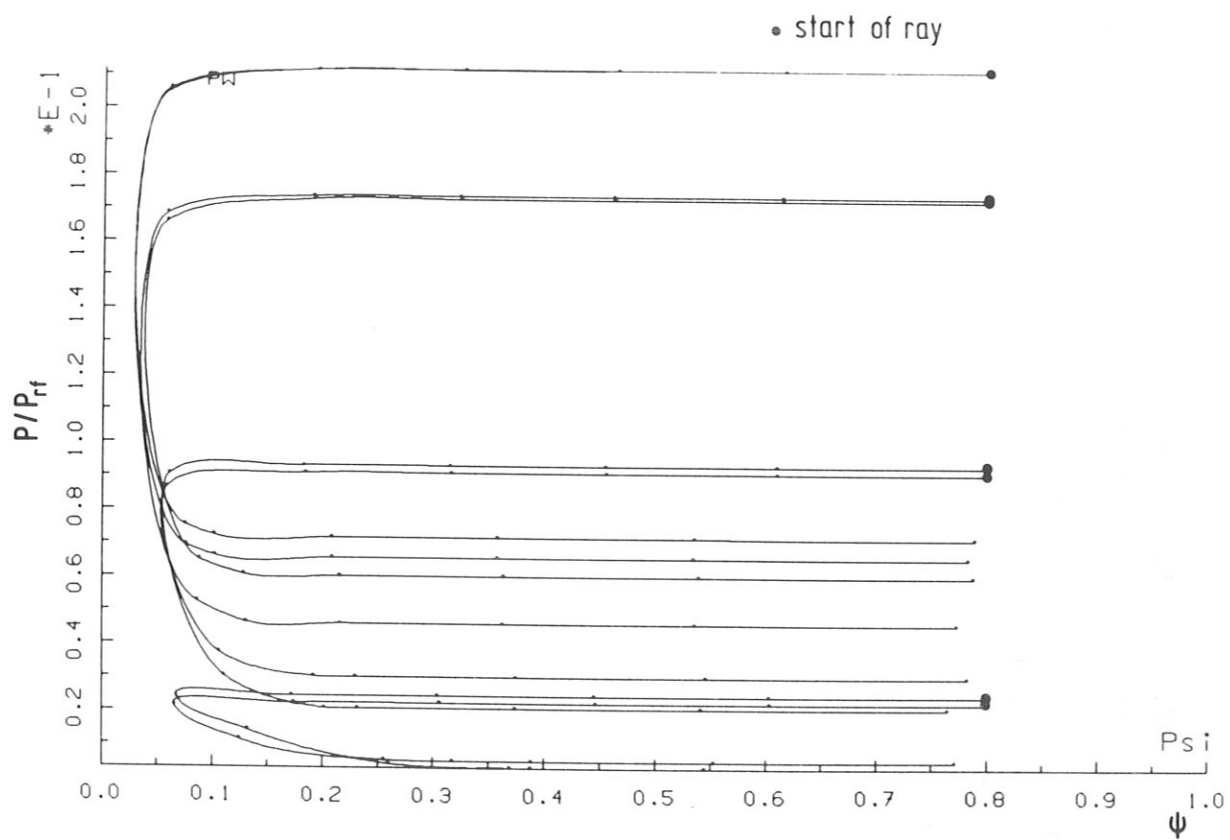


Fig.A10: Transported power of each ray versus ψ .

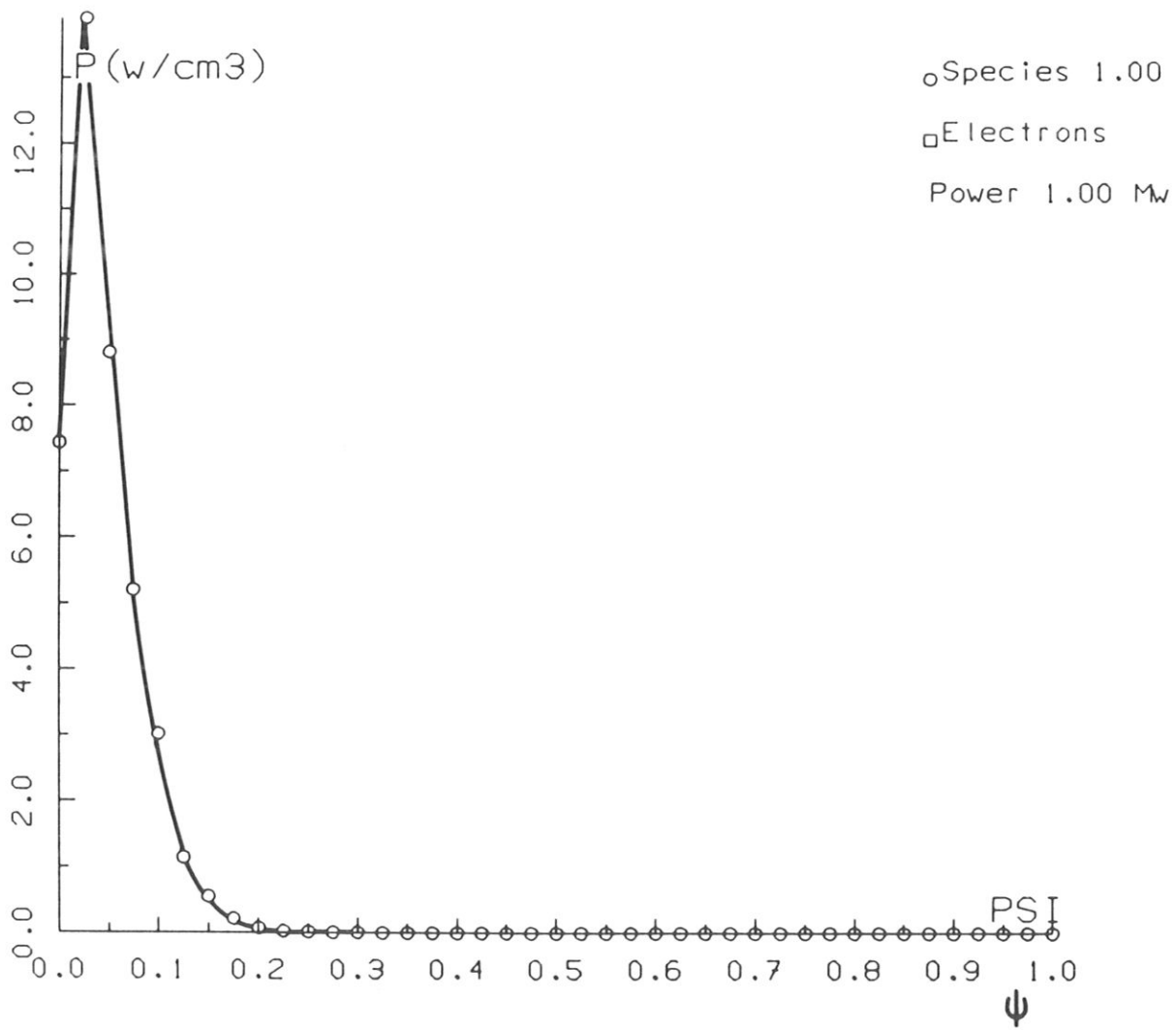


Fig.A11: Power deposition for electrons and ions versus ψ (note: for $n_\phi = 12$ all power is absorbed by ions, no electron profile exists).